THE HONG KONG POLYTECHNIC UNIVERSITY
香港理工大學
Pao Yue-kong Library
包玉剛圖書館

Copyright Undertaking

This thesis is protected by copyright, with all rights reserved.

By reading and using the thesis, the reader understands and agrees to the following terms:

1. The reader will abide by the rules and legal ordinances governing copyright regarding the use of the thesis.
2. The reader will use the thesis for the purpose of research or private study only and not for distribution or further reproduction or any other purpose.
3. The reader agrees to indemnify and hold the University harmless from and against any loss, damage, cost, liability or expenses arising from copyright infringement or unauthorized usage.

IMPORTANT

If you have reasons to believe that any materials in this thesis are deemed not suitable to be distributed in this form, or a copyright owner having difficulty with the material being included in our database, please contact lbsys@polyu.edu.hk providing details. The Library will look into your claim and consider taking remedial action upon receipt of the written requests.

Pao Yue-kong Library, The Hong Kong Polytechnic University, Hung Hom, Kowloon, Hong Kong

http://www.lib.polyu.edu.hk

This thesis in electronic version is provided to the Library by the author. In the case where its contents is different from the printed version, the printed version shall prevail.

The Hong Kong Polytechnic University

Department of Applied Physics

Fabrication and Characterization of ZnO-based Light-emitting diodes

Luk Chi Man

A thesis submitted in partial fulfillment of the
requirements for the degree of Master of Philosophy

August, 2011

Certificate of originality

I hereby declare that this thesis is my own work and that, to the best of my knowledge and belief, it reproducers no material previously published or written, nor material that has been accepted for the award of any other degree or diploma, except where due acknowledgement has been made in the text.

____________________________________ (Signature)

___**Luk Chi Man**_____ (Name of candidate)

Abstract

Nowadays, solid-state lighting devices based on wide band gap semiconductor have attracted considerable attention. Efforts are being made in order to achieve light-emitting diodes (LEDs) with high efficiency, high colour gamut and low heating output. Along this direction, zinc oxide (ZnO) is one of the promising semiconductors because of its wide band gap (3.37 eV) and relatively large exciton binding energy (60 meV). In addition, ZnO possesses a number of intrinsic and extrinsic radiative defect levels which exhibit a wide emission range covered from ultraviolet to visible, leading to the potential application of white LEDs.

In the present study, a series of undoped ZnO and aluminium (Al)-doped ZnO thin films were prepared by filtered cathodic vacuum arc (FCVA) technique. The electrical, optical and structural properties of the ZnO films were investigated as functions of substrate temperature and doping concentration. The ZnO films exhibited c-axis orientation. It is revealed that the resistivity decreased as the substrate temperature increased from room temperature to 400℃ due to enhanced crystallinity and larger grain size. In addition, all the ZnO films have an optical transmittance of over 80% in the visible spectrum. The blue-shifted photoluminescence (PL) peak of the ZnO with increasing Al doping concentration will be discussed.

With the optimized growth parameters, n-ZnO:Al/i-ZnO/p-GaN:Mg heterojunction LEDs were fabricated. The electrical characteristics of the diodes were investigated. The ultraviolet (UV) electroluminescence (EL) from the device was detected at room temperature. The emission is attributed to the electron-hole radiative recombination in the ZnO region and is explained in detail by an energy band diagram.

ZnO nanostructures are expected to have improved optical and electronic properties because of the quantum confinement effect. Using low-temperature aqueous chemical method, the ZnO nanorods arrays were grown on the buffer layers prepared at various temperatures. The nanorods were grown along [0001] direction. The PL measurement indicated that the emission spectrum covered a UV peak at ~ 380 nm and a broad visible band at ~ 560 nm. The PL spectra of the ZnO nanorods are independent on the growth temperature of the buffer layer. Moreover, the buffer-layer-thickness-dependent structural and optical properties were studied.

The as-grown ZnO nanorods were utilized to fabricate hybrid LED with an organic semiconductor, N, N'-diphenyl-N, N'-bis(1-naphthyl)-1, 1'-biphenyl-4, 4'-diamine (*α*-NPD), which is one of the most widely used hole transport and blue-emitting organic semiconductors. Current-voltage characteristics of the devices exhibited nonlinear rectifying behaviour. The EL spectra of the hybrid LEDs reveal a blue and broad yellowish green emission originated from the *α*-NPD layer and the defect levels of the ZnO respectively. The origin of the emission bands from the hybrid structures will be examined.

List of publications

Journal articles:

1. J. Ye, (Y. Zhao), L. B. Tang, (L. M. Chen), C. M. Luk, S. F. Yu, (S. T. Lee) and S. P. Lau, Ultraviolet electroluminescence from two-dimensional ZnO nanomesh/GaN heterojunction light emitting diodes, Applied Physics Letters 98(2011) 263101.

Conference papers:

1. C. M. Luk and S. P. Lau, Ultraviolet electroluminescence from n-ZnO:Al/i-ZnO/p-GaN:Mg heterojunction light-emitting diodes, OSA-IEEE-COS Topical Meeting on Advances in Optoelectronics and Micro/Nano-Optics 2010.
2. C. M. Luk, Y. Y. Hui, J. Ye, P. K. L. Chan and S. P. Lau, Hybrid light-emitting diodes based on low-temperature grown ZnO nanorods and organic semiconductor, International Conference on Materials for Advanced Technologies 2011.

Acknowledgment

I would like to thank my supervisor Prof. S. P. Lau for his professional and invaluable advices in my MPhil study. His broad view, deep insight and opinions helped me a lot through difficulties in my research and study. I also wish to thank Dr. W. Lu, Mr. M. N. Yeung and Mr. C. S. Lo for their assistant of experimental measurements.

My special thanks are also given to my colleagues for providing me with help and support throughout my study. They include Dr. J. Ye, Dr. G. Tai, Dr. L. B. Tang, Dr. L. Lei, Mr. C. S. Wei, Mr. Y. Y. Hui, Mr. S. T. F. Lee, Miss M. K. Lau, Miss S. M. Ng, Mr. H. F, Wong, Mr. K. Wang, Mr. A. Q. Jian, Mr. Z. H. Sun, Mr. Q. D. Tai, and Mr. N. Wang.

Last but not least, I truly appreciate the continued encouragement, endless supports and understanding from my parents and my wife Miss Yeda Tsoi during my research study. They have been inspiring me at every moment.

Table of contents

List of figures

List of tables

Chapter 1 Introduction

1.1 Wide band gap semiconductors

After the first generation of the semiconducting electronic material for silicon (Si), a great amount of effort has been made to develop other kinds of semiconductors. The most common example is the III-V compound semiconductors. These compounds, including GaAs, GaP, InP and their alloys, open a potential market in high performance optoelectronic devices as well as digital systems [1].

The next generation of semiconducting materials is emerging from research areas which focus on the wide band gap semiconductors. Such materials have band gap energies greater than 2.3 eV (comparing with Si, ~ 1.1 eV). The examples of these semiconductors are silicon carbide (SiC), aluminum nitride (AlN), gallium nitride (GaN), zinc oxide (ZnO) and zinc selenide (ZnSe).

The devices utilized the wide band gap will have an improved operating characteristics comparing with those made from Si and GaAs, especially at high-power and high-temperature applications. The materials with wide band gap energies have usually high operating temperature because of the contribution from the intrinsic carrier concentration [2]. The intrinsic carrier concentration at high temperature depends on the band gap energy:

$$n_i = \sqrt{N_C N_V} exp\ (\frac{-E_g}{2kT})$$

where n_i is intrinsic carrier concentration, N_C effective state density in the conduction band, N_V is effective state density in the valence band, E_g is band gap energy, *k* is Plank's constant and *T* is absolute temperature. The intrinsic concentration in wide band gap energy reached limit at higher temperature. Therefore, wide band gap semiconductors have the potential to operate at high temperature. In addition, devices made from the wide band gap semiconductors can be used for the short-wavelength emitter, such as blue light-emitting diodes (LEDs), UV LEDs, UV laser diodes, UV detector and other devices.

1.2 General properties of ZnO

ZnO is a direct band gap semiconductor. It has a wurtzite hexagonal structure, which is similar to GaN, a widely used UV photonic material. The lattice constants of a-axis and c-axis are 0.324 nm and 0.517 nm respectively. It is a very stable semiconductor even at the temperature near its melting point at ~ 1975 ℃, making ZnO stable in device processing at high temperature. ZnO is able to grow at relatively low temperature because of self-assembly mechanism. Therefore, it can directly grow on different types of substrates, including crystalline and amorphous substrates. Moreover, ZnO has a wide band gap of ~ 3.37 eV at room temperature. Indeed such optical properties can be utilized for the short wavelength optoelectronic applications such as including LEDs, laser diodes (LDs) and UV detectors. Actually, ZnO has a number of advantages over GaN. The growth temperature of ZnO is lower than that of GaN. ZnO has a higher exciton binding energy (60 meV) than GaN (28 meV). This exciton binding energy is useful for the efficient UV optoelectronic application at room temperature (kT = 26 meV). In addition, the larger exciton binding energy than thermal energy at room temperatures ensures that the excitonic emission is significant at room temperature or well above room temperature. As a result, the practical lasers with low thresholds at high operating temperature are possible. Moreover, the optical gain in ZnO (300 cm^{-1}) is higher than GaN (100 cm^{-1}) at room temperature. The low-threshold UV lasing of bulk ZnO at low temperature and thin films at room temperature [3-5] have been reported.

ZnO is more resistant to radiation damage than GaN, indicating the potential for space-based applications [6]. ZnO can also be easily etched by acid thus wet chemical processing is possible. Table 1 summarizes the properties of ZnO and the typical wurtzite structure is illustrated in Fig. 1.1.

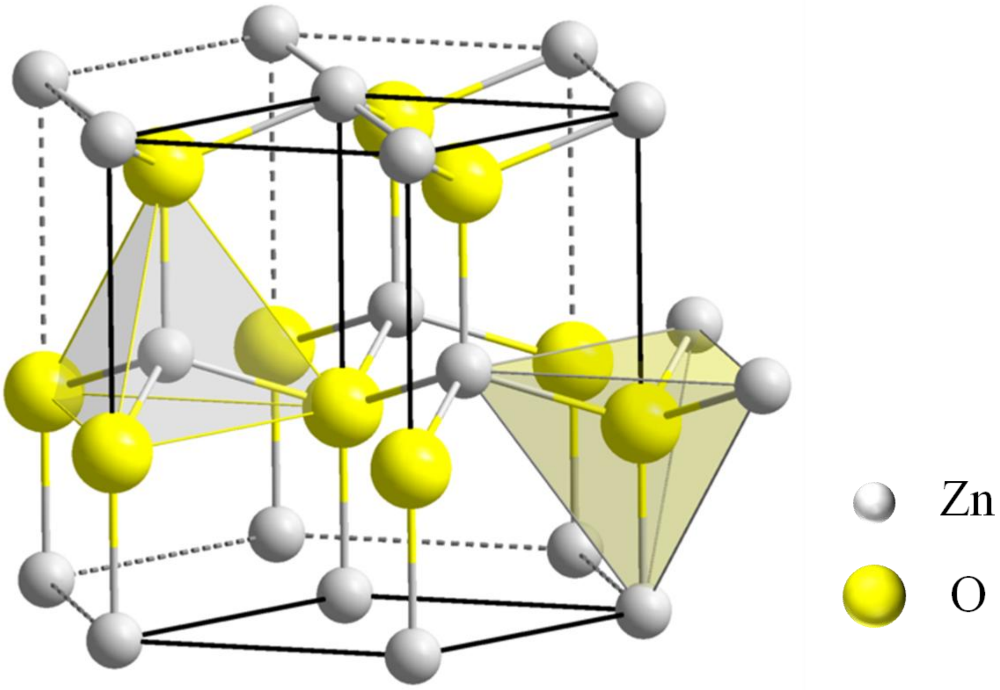

Figure 1.1 Wurtzite structure of ZnO.

Physical property	Value
Lattice constant at 300 K	
a	0.32495 nm
c	0.52069 nm
c/a	~ 1.602 (for ideal hexagonal structure, 1.633)
Density	5.606 g/cm^3
Melting point	1975 ^{o}C
Heat capacity	0.494 J/gK
Linear expansion coefficient	a = 6.5 x 10^{-6} /^{o}C
	c = 3.0 x 10^{-6} /^{o}C
Static dielectric constant	8.656
Refractive index	2.008, 2.029
Energy band gap at 300 K	3.37
Exciton binding energy	60 meV
Exciton Bohr radius	2.03 nm
Intrinsic carrier density	< 10^6 cm^{-3}
Electron effective mass	0.24 m$_o$
Electron Hall mobility at 300 K for low n-type conductivity	200 cm^2/Vs
Hole effective mass	0.59 m$_o$
Hole Hall mobility at 300 K for low p-type conductivity	~ 5 to 50 cm^2/Vs

Table 1-1 General properties of ZnO [7].

1.3 Doping of ZnO

The intrinsic ZnO is unintentionally n-type conduction. It is widely believed that the intrinsic defects are mainly originated from zinc interstitial (Zn_i) and oxygen vacancy (V_O), which are generally the sources of donors in ZnO. In recent years, there has been a controversy about the dominant native shallow donor in ZnO. The previous research [8] showed that the Zn_i is dominated in shallow donors rather than V_O. On the other hand, it was recently reported that hydrogen atoms can act as hydrogen-related donors [9] such as hydrogen substitution (H_O) and hydrogen interstitial (H_i) [9, 10].

Intentional n-type doping of ZnO can be accomplished by using group III, IV, VI and VII elements. Among these elements, group III elements such as Al, Ga and In are the common materials to substitute Zn ions. Doping with Al [11], Ga [12] and In [13], it can produce high conducting n-type ZnO with the carrier concentration as high as $> 10^{20}$ cm^{-3}. Many research groups have attempted Al and Ga doping for electron injector in LEDs and transparent ohmic contacts.

As for p-type doping, it still remains a challenge. The most important concern is to fabricate p-type ZnO with low resistivity and high carrier concentration. Since ZnO intentionally shows n-type properties, the acceptors may be self-compensated by native defects such as Zn_i and V_O. In order to grow p-type ZnO, large amount of efforts have been devoted to make higher acceptor concentration than the unintentional donor concentration. The acceptors in ZnO mostly include group I elements such as Li [14-16], Na [17], Ag [18] and group V elements such as N [19], P [20], As [21,22], Sb [23]. It is possible to substitute either group I elements for Zn sites, or group V elements for O sites. In spite of difficulty in p-type doping, ZnO-based homojunction LEDs have been demonstrated in recent years [24-27], and the results achieved so far are valuable and encouraging. This will be described in more detail in Chapter 2.

1.4 Motivation

At present, many works have been reported on the fabrication and characterization of ZnO thin films. In order to realize the ZnO-based optoelectronic devices, however, several key issues must be understood and overcome. The challenges include the fabrication of the device-quality films, enhancement of the electrical conduction and doping for n- and p-type conductivity.

Apart from thin films, it has been reported that the utilization of ZnO nanostructures can improve significantly the performance of optoelectronics devices such as transistor, solar cells and LEDs. Even the growth condition and properties of ZnO nanostructures have been extensively studied, the relationship between the growth conditions and optical properties is still uncertain.

This project aims at fabricating ZnO and Al doped ZnO thin films. The structural, electrical and optical properties of the films as a function of the growth condition have been investigated systematically. By finding the optimized growth conditions, the ZnO films were used to fabricate heterojunction LEDs. Besides, ZnO nanorods have been synthesized by a low-temperature aqueous method. The structural and optical properties of the nanorods have been studied against the buffer layer thicknesses and the growth temperatures of the buffer layers. Hybrid LEDs utilizing ZnO nanorods and organic semiconductor were fabricated.

1.5 Thesis overview

In Chapter 1, an introduction of wide band gap semiconductor and ZnO is provided. The doping of ZnO is introduced as well. The motivation of this project is also included.

In Chapter 2, a wide range of ZnO fabrication methods are briefly introduced. Various ZnO nanostructures and their fabrication approaches are presented. The working mechanism of LED will also be introduced.

The experimental and characterization details are described in Chapter 3. The filtered cathodic vacuum arc (FCVA) technique is also introduced in this chapter.

In Chapter 4, the structural, electrical and optical properties of the ZnO and ZnO:Al films as a function of growth condition are studied. The effects of doping concentration on the electrical and optical properties of the ZnO:Al films are discussed.

In Chapter 5, heterojunction LEDs based on ZnO:Al, ZnO and p-GaN:Mg has been demonstrated. The origin of the emission is discussed.

The fabrication of the ZnO nanorods is presented in Chapter 6. The setup for the nanorods growth will be included. The structural and optical properties of the as-grown ZnO nanorods with different buffer layer thicknesses and deposition temperatures are investigated in this chapter.

In Chapter 7, hybrid LEDs based on the ZnO nanorods and organic semiconductor are demonstrated.

In Chapter 8, the findings of the ZnO thin films and nanorods are concluded and the future work is discussed.

Chapter 2 Literature review

2.1 ZnO thin films

ZnO has been widely used in both industry and research area for several decades. As mentioned in Chapter 1, it possesses several properties including semiconductor, luminescent, photoconductivity and photochemical behaviors. Hence, a wide range of applications such as piezoelectric transducers, sensors, heat mirror and surface acoustic wave devices, etc. are available.

The first fabrication of ZnO films with wurtzite structure was reported in 1983 using CO_2 laser ablation of ZnO powder target [28]. The ZnO films exhibited high (0002) orientation with smooth surface and good optical transparency. Subsequently, high quality single crystalline ZnO grown by vapor-phase [29], melt method [30] and hydrothermal [31] have been reported. Other deposition approaches, including evaporation [32], sputtering technique [33], chemical vapor deposition [34], molecular beam epitaxy (MBE) [35], pulsed laser deposition (PLD) [36], sol gel method [37] and ion-assisted reactive deposition [38] have also been successfully developed.

In the pursuit of growing high-quality ZnO thin films, vacuum arc deposition technique was reported in the recent year. This technique is realized by directing the arc plasma onto substrate that is generally placed normal to the plasma flow direction. Tetrahedral amorphous carbon (ta-C) [39], carbon nitride (CN) [40], aluminum oxide (Al_2O_3) [41] and other metallic and oxide films are prepared by this technique. The deposition temperature can be as low as 50-400 ^{o}C, or even at room temperature. The principle of the vacuum arc is based on the concentration of the current at the cathodic spots when electrical discharge occurs. These cathodic spots consist of electrons, metal atoms and microsized droplets of the cathode materials with extremely high current density. The plasma is then produced at the non-stationary cathode spots, following by the plasma expansion from the cathode spots in the vacuum [42]. Generally, the plasma beam has a high ion energy ranged from 20-100 eV, depending on the cathode materials and ion mass. The high ion energies of the condensing atoms are one of the significant features of vacuum arc deposition and it is critically important to the materials properties of the deposited film because it provides a pseudo temperature for film growing. Hence, it results in high film quality because of the enhanced surface atom mobility and high adhesion energy. By controlling the ion energy, films morphology and structure can be optimized [43].

In addition to the high ion energy, high ionization and multiple ion charge states are also critical to the vacuum arc deposition. The cathode material in the plasma beam is normally fully ionized and it allows the formation of a relatively high fraction of multiple-charged ions. The distribution of the ion charge states can be adjusted by magnetic fields, current transients and arc current [44]. It had been reported that the enhancement of the ions charge states can be achieved by increasing the arc voltage utilizing the transient processes that accompany arc current spike [45]. Exploiting the vacuum arc deposition, the ZnO and Al doped ZnO films were deposited by filtered cathodic vacuum arc technique in this project. The detail of the deposition system is described in Chapter 3.

2.2 ZnO nanostructures

Due to the development of science and technology, considerable research efforts have been put at synthesizing materials in nanometer scale. Understanding the physical and chemical properties related to low dimensionality helps explore their possible applications in nanoelectronic devices.

Nanotechnology is not only a simple process for miniaturization from micro-meter scale down to nanometer scale. Materials in nanoscale exhibit unique physical properties owing to size dependent effect. The example is the variation of band gap energy of semiconductors with materials dimension. In order to realize the novel properties and potential applications, the fabrication of nanostructures become very important. There are two approaches for synthesizing nanostructure: top-down and bottom-up. The former refers to milling and attrition in making nanoparticles while the latter to the build-up of materials atom by atom on the basic unit.

A variety of ZnO nanostructure morphologies have been reported, such as nanowires, nanorods, nanobelts, nanoribbons and tetrapods [46]. Fig. 2.1 shows some examples of the morphologies of ZnO nanostructures. The fabrication of ZnO nanostructures can be divided into two types. The first type is spontaneous growth approach. In this approach, the nanostructures are synthesized without any template, but by using metal catalysts or self-catalyzed. The most common used metal catalyst is Au, which provides advantage for aligned and selective area growth [47]. Another approach is a template-based synthesis. Before the growth, a porous template, for example, an alumina is prepared on the substrate. The well-aligned nanowires or nanorods are synthesized within the voids, and then the template is etched. In other words, the diameters and lengths of the nanowires depend on the size of the void. Aligned nanorods can also be obtained by hydrothermal method without any metal catalyst [48]. The degree of alignment and the aspect ratio is shown to be dependent on the seed layer used and the fabrication condition such as growth time and temperature [49]. On the other hand, the growth of ZnO nanostructures by vapor deposition is typically influenced by temperatures of the source and the substrate, source-to-substrate distance, the heating rate and gas flow rate. The effects of these factors on the ZnO morphologies have been studied [50].

Other chemical route methods including sol-gel and biomineralization methods were also used to fabricate ZnO nanowires [51-53]. Brien et al. reported a new approach for the growth of ZnO nanorods by thermal decomposition of zinc actate inorganic solvent in the presence of oleic acid [54]. This method can produce relatively monodisperse ZnO nanorods with the length of 40-50 nm and diameter of ~ 2 nm.

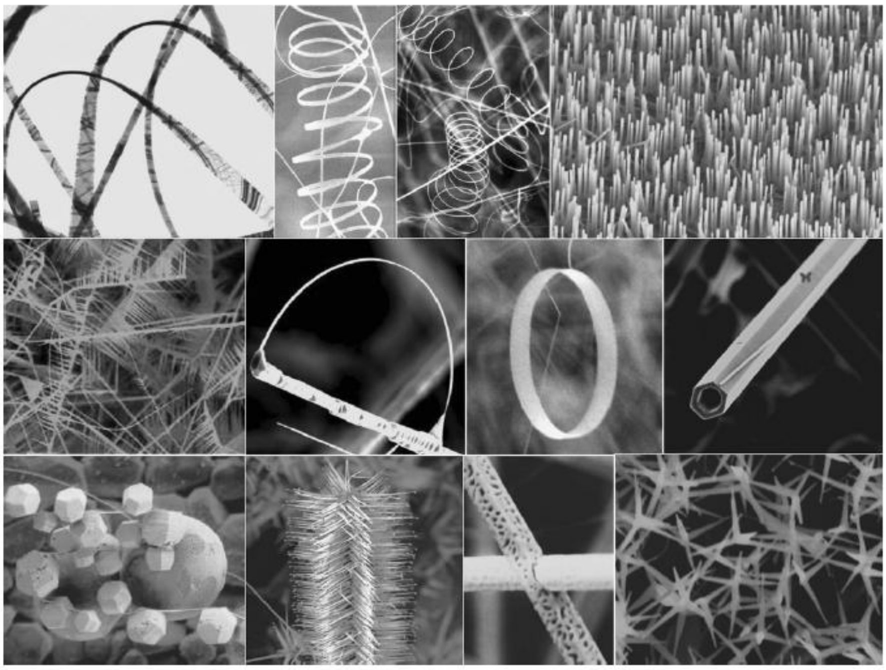

Figure 2.1 Representatives of ZnO nanostructures [55].

2.3 Development of ZnO-based light-emitting diodes

During the past decades, ZnO-based materials have been emerged as promising materials for optoelectronic devices from the UV to visible range. At the early stage, several studies have been conducted to investigate the potential semiconductors such as GaN, ZnO, SiC and ZnSe for solid-state lighting. The first ZnO-based LED was reported in 1974 using metal-insulator-semiconductor (MIS) configuration [56]. The sample used in their experiment was made from single crystal ZnO grown by hydrothermal synthesis, and the SiO acted as an insulating layer. With the continuous development, several approaches have been realized to fabricate the ZnO-based LEDs.

2.3.1 Homojunction LEDs

In spite of the difficulty of p-type doping of ZnO, ZnO-based p-n homojunction LEDs is the most concerned issue for the fabrication of high efficiency devices. In 2000, Aoki et al. [57] reported the first homojunction LEDs. In their work, p-type ZnO was made by thermal evaporation of Zn3P2 onto the ZnO single crystal substrate, and followed by the laser annealing under the nitrogen atmosphere in order to make P atoms diffuse into ZnO. Their homojunction LEDs can emit weak UV and greenish-blue bands. However, it is difficult to control the doping concentration of the ZnO in this approach. Xu et al. [58] demonstrated the growth of the p-type nitrogen-doped ZnO on the ZnO substrate by plasma-assisted MOCVD. Diethyl zinc was used as the source of the zinc and NO plasma acted as the sources of O and N. Room temperature EL of their LEDs exhibited a weak UV emission peaked at ~ 375 nm and a broad emission at ~ 450 nm. Despite of the encouraging results; there is still a comparable room for improvement.

2.3.2 Heterojunction LEDs

In order to avoid the p-type doping of ZnO, other p-type semiconductors such as GaN, p-Si, 4H-SiC and other conducting oxides are employed to form ZnO-based p-n junction LEDs. Among them, GaN-based material is the most common used p-type semiconductor because of the smaller lattice mismatch (< 1.8 %) of ZnO. Due to the compatibility of these two materials, ZnO/GaN heterostructure have been exploited beyond LED application. However, there have been also several attempts to fabricate the heterojunction LEDs by depositing p-type ZnO on various n-type semiconductors. Mandalapu et al. [59] fabricated heterojunction LEDs by depositing Sb doped p-type ZnO on the n-type Si substrate. Hwang et al. [60] reported on the growth and device properties of p-ZnO/n-GaN heterojunction LEDs on a (0001) sapphire substrate.

2.3.3 p-i-n heterojunction LEDs

To improve the optical characteristics, a thin single crystal or insulating layer was inserted in the p-n junction. Tsukazaki and co-workers [61] demonstrated p-ZnO:N/i-ZnO/n-ZnO:Ga heterojunction LEDs by MBE technique in 2005. The ZnO layer acted as an emission layer for the devices. However, the UV emission was very weak. In 2006, J. G. Lu et al. used ZnCdO film as an intrinsic layer to fabricate ZnO-based p-i-n heterojunction LEDs. The reason of using ZnCdO is due to the narrower band gap energy as compared to the n- and p- type ZnO so that it can increase the probability of electron-hole recombination within that layer. In addition, double and triple heterojunction LEDs were demonstrated. Ohashi et al. [62] reported a ZnO-based double heterojunction LEDs which consisted of n-type ZnO cap layer, n-type $Mg_{0.12}Zn_{0.88}O$ cladding layer, n-type $Zn_{1-x}Cd_xO$ emission layer and and p-type N doped $Mg_{0.12}Zn_{0.88}O$ on 4H-SiC substrates. The red emission peaked at ~ 650 nm was appeared at the current of 120 mA. Osinsky et al. [63] fabricated an MgZnO/ZnO/AlGaN/GaN triple heterostructure and a UV emission was obtained at ~ 390 nm which was attributed to the recombination at the ZnO/AlGaN interface.

2.3.4 ZnO-based multi-quantum well LEDs

The multi-quantum well structure effectively limits non-radiated recombination and confined the electron-hole pairs. Ryu et al. [25] demonstrated ZnO-based LEDs that employed seven quantum wells composed of $Be_{0.2}Zn_{0.8}O$/ZnO well layers. The EL of the devices located at ~ 363 nm, ~ 388 nm and 550 nm. The primary emission was originated from the localized exciton emission in the quantum wells and the secondary peak was from the impurity-bound exciton emission in ZnO.

Chapter 3 Experimental and Characterization Methods

3.1 Filtered cathodic vacuum arc (FCVA) technique

The vacuum arc is a plasma discharge between two metallic electrodes in vacuum. The plasma generated by the arc has a large concentration of metal ions. The origin of vacuum arc deposition was first purposed by Thomas Edison in 1892 [64]. The first "modern" study of the properties of metal coatings deposited from vacuum arc was initiated by Kikishi et al in 1965 [65]. Subsequently, the interest in cathodic arc deposition as an alternative technique arises greatly to understand the plasma process and its properties related to high quality films growth.

In addition to the generation of plasma, the arc discharge also produces small droplets referred to macroparticles due to their large mass compared with the ionized plasma. These macroparticles may prevent the application of the arc deposition process to the areas of optical and microelectronics. To reduce or eliminate macroparticles, considerable efforts have been made in the past decades. Brandolf [66] suggested the use of a shield which is placed between the substrate and arc source. It was found that the number of macroparticles decrease although the growth rate is low. To improve the efficiency of macroparticles removal, Aksenov et al. [67] designed a magnetic filter in the cathodic vacuum arc system. The plasma is guided by a curved magnetic filter to the substrate located beyond the line-of-sight of cathode. Macroparticles move along almost line-of-sight trajectories due to their inertia and therefore they will be separated from the plasma and removed through the magnetic filtering. The recent development of magnetic filter is to use off-plane double bend filter, which consists of a stainless steel quarter torus with a copper coil wound outside, allowing non-line-of-sight path between the arc source and the substrate [68, 69]. To date, this deposition technique is well known as filtered cathodic vacuum arc (FCVA).

There are several advantages of FCVA over other deposition techniques. The high kinetic energy of deposition species makes the film self-densification so that the film can be grown at low temperature, or even at room temperature. The FCVA is available for large area deposition with a careful control of plasma. The films prepared by FCVA exhibit excellent adhesion and high density. Moreover, FCVA technique is based on ion beam deposition by which no by-products are made on the substrates. This technique is currently well recognized as a cost effective and prevailing deposition technique of a wide range of application from microelectronics to protective coatings.

The schematic diagram of an off-plane double bend FCVA system is depicted in Fig. 3.1. The system mainly consists of three parts. They are cathodic arc source, plasma-filtering duct and deposition chamber. The cathodic arc source contains power supply, arc trigger, cathode, the target and target cooling system. An electromagnetic field coupled with the radial electric field on the toroidal duct is formed to confine and guide the plasma to the substrate and filter out the macroparticles. During the deposition, the chamber is pumped down to the desired pressure by rotary and turbo pump system.

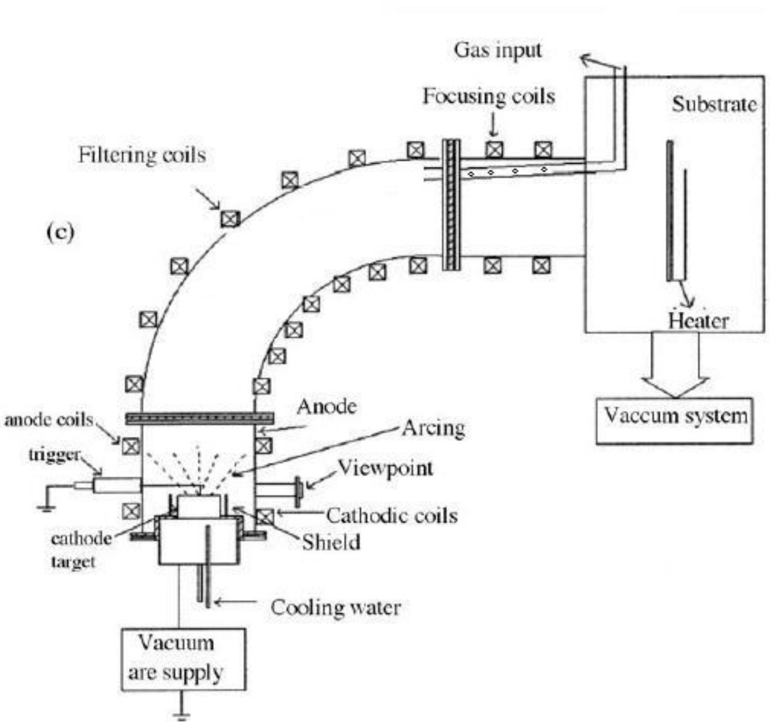

Figure 3.1 Schematic diagram of FCVA system.

Zn and ZnAl (with 5 and 7 at% of Al) alloy targets were used as the cathodic materials and high purity (99.99%) oxygen gas was used as a reactant gas. Before the deposition, the chamber base pressure was kept at about 5 x 10^{-6} Torr. When the arc trigger is struck on the metallic target with an arc current of 50 A, energetic plasma ions are formed from the metallic target. The plasma ions are steered by a magnetic field produced by the copper coils wrapped around the filter. During the deposition, the magnetic field was kept at ~ 15 mT. Oxygen is introduced into the chamber near the filtering duct so that the metal-oxide plasma can be formed. The oxygen flow rate was monitored by a mass flow meter. The oxygen partial pressure in the deposition process is kept at 2.0 mTorr. The ZnO and ZnO:Al films were prepared at substrate temperatures ranging from room temperature to 400℃.

3.2 Characterization methodology

3.2.1 X-ray diffraction (XRD)

X-ray diffraction (XRD) is one of the most widely used non-destructive techniques for characterizing crystalline materials, which provides information on structures, phases and preferred crystal orientations. All the XRD measurements were carried out by Cu Kα (wavelength = 0.154 nm) radiation on Bruker D8 Advanced X-ray diffractometer with an accelerating voltage and current of 40 kV and 40 mA, respectively. The films were characterized by θ-2θ scan mode. In this mode, the position of X-ray source is fixed. When the sample on the stage rotated through an angle of θ, the detector scans over an angle of 2θ correspondingly. The interplanar spacing d and the diffraction angle θ can be related by Bragg's diffraction equation

$$\lambda = 2d \sin\theta$$

where λ is the wavelength of X-ray. For hexagonal structure, the relationship between the interplanar spacing and lattice constant a and c is given by:

$$a = d_{hkl}\sqrt{\frac{4}{3}(h^2 + hk + k^2) + l^2(\frac{a}{c})^2}$$

3.2.2 Film thickness measurement

The thickness of all the ZnO and ZnO:Al films were measured by an α-step surface profiler (KLA-Tencor P-10) which has a resolution of 1 nm. This system is used to measure the height of a small step which is not more than 3 μm. By moving the stylus horizontally, it experiences a sudden drop (or rise) at the edge such that the electrical signal is generated and detected. The displacement is determined via the calibration process. The applied load of the stylus should be very low in order to avoid damaging the film surface. The schematic diagram of the surface profiler is shown in Fig. 3.2.

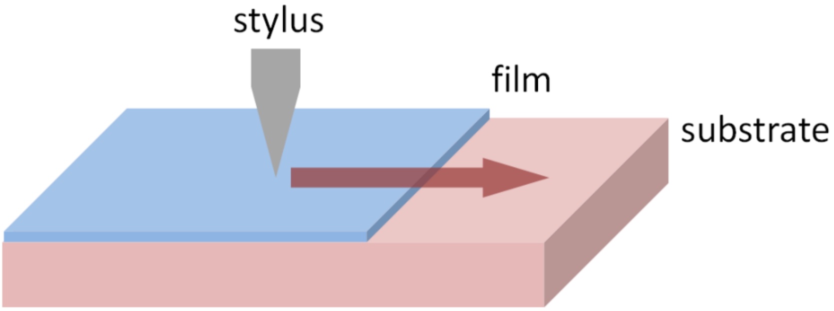

Figure 3.2 Schematic diagram of the surface profiler.

3.2.3 Scanning electron microscopy (SEM)

In surface morphology studies, scanning electron microcopy (SEM) is a useful technique for material characterization because of large depth of field and high magnification power. In our project, field emission scanning electron microscopy (FESEM) – JEOL JSM-633F was used for examining the cross section of the thin films and morphology of the as-grown nanorods. The SEM images are obtained from secondary electrons detection. The secondary electrons are detected by Everhart-Thornley detector. The accelerating voltage used is 5 kV. Since ZnO is a semiconductor which can conduct electricity, gold coating is not necessary.

3.2.4 Transmission electron microscopy (TEM)

Transmission electron microscopy (TEM) is one of the precise techniques for microstructure characterization of thin films as well as nanostructures. It generally provides information on size, shape and arrangement of atoms within the sample. TEM consists of an electron gun, objective lens and condenser lens. High-speed electrons emit from the electron gun when applying extremely high accelerating voltage. The condenser-lens system is used to adjust the electron illumination uniformly on the specimen. After passing through the condenser lens, a first image is formed by objective lens, followed by further magnification from intermediate and projector lenses. An entire image is then formed on the fluorescent screen. In this work, the detailed study of nanorods was performed by using JOEL JEM-2010 Electron Scanning microscope operating at 200 kV.

3.2.5 Atomic force microscopy (AFM)

The surface roughness and crystal size of the thin films can be revealed by using atomic force microscopy (AFM) (Nanoscope IV AFM). The working principle of AFM is based on the intermolecular force between the tip and the specimen surface. The schematic diagram of an AFM setup is shown in Fig. 3.3. The AFM consists of a sharp tip at the end of a flexible cantilever, which places several nanometers above the sample surface. The coordinate of the tip is determined by a laser source connected by a photodiode. When the tip is scanning along the surface, the cantilever deflects due to the roughness. The tip-surface interaction is monitored by reflecting laser beam off the back of cantilever into the photodiode detector. The photodiode records the change of the spot position and hence results in difference of output voltage, following by the determination of the oscillation amplitude. There is a feedback circuit to maintain a constant separation between the tip and surface in order to avoid the damage of both the tip as well as the sample.

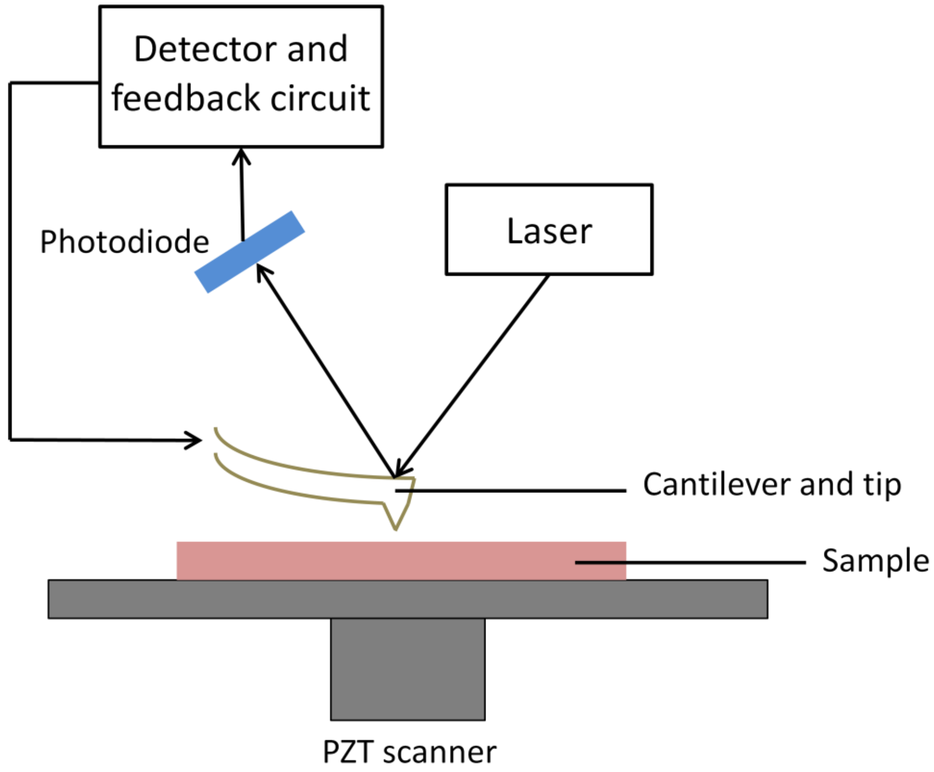

Figure 3.3 Schematic diagram of the AFM.

3.2.6 Hall effect measurement

The importance of the Hall effect is emphasized by the determination of carrier concentration, mobility of carriers and the electrical resistivity in semiconductors. The theory of Hall effect is based on the Lorentz force characteristics of a charged carrier. When the free carriers (electrons or holes) are experienced an electric field, the carriers move by the electrostatics force. A magnetic field is applied perpendicular to the moving charges, inducing a Lorentz force which makes the trajectory of the carriers bending. The Lorentz force drives and accumulates the carriers to one side. The Hall voltage can be determined when we measure the potential difference across the two edges of the sample. Once the Hall voltage is defined, the resistivity, carrier density and mobility in the semiconductor can be calculated accordingly. In this project, the transport properties of the ZnO and ZnO:Al films were studied using van der Pauw method by Hall effect measurement system (ECOPIA AMP-55) at room temperature. Prior to measurement, the indium contacts were placed at the four corners of the samples and the Ohmic characteristics of the samples were tested.

3.2.7 Transmittance

Transmittance of the thin films was measured by a Shimadzu UV-2100PC UV-VIS Scanning Spectrophotometer. The spectrophotometer has a broad light source wavelength ranged from 200 nm to 900 nm. The transmittance T can be calculated by the ratio of transmitted intensity I to incident intensity I_o,

$$T = \frac{I}{I_o}$$

From the transmittance spectrum, the absorption coefficient α can be converted by the following equation,

$$\alpha = -\frac{1}{d} ln\, T$$

where d is the thickness of the film.

Since the band gap energy E_g and absorption coefficient has the following relationship,

$$\alpha \sim \sqrt{E - E_g}$$

E_g can be estimated by plotting $(\alpha hv)^n$ against photon energy hv and extrapolation of the curve to $(\alpha hv)^n = 0$. The value of n is dependent on the transition mechanism. n can be 0.5 and 2 for indirect and direct transition energy bands respectively.

3.2.8 Photoluminescence (PL)

Photoluminescence (PL) is an important technique to study the electronic band structure and measure the purity of semiconductors. In the process, the specimen is excited to higher energy state by absorbing photons. Then it relaxes to a lower energy state and re-radiates photons. The radiation of the specimen depends on the band gap energy. The PL system used is a fluorescence spectrometer (Edinburgh Instrument) with a model of FLSP920. The samples were excited by a continuous Xenon lamp (at 324 nm) at room temperature. The radiative emission was obtained from the samples surface, and was detected by PMT detector (Model: R928) with a spectral range from 200 to 870 nm.

Chapter 4 Characterization of the ZnO and ZnO:Al thin films

4.1 Effects of substrate temperature

4.1.1 Structural properties

It is well known that ZnO films are highly textured with the c-axis orientation perpendicular to the surface of the substrate. The XRD results indicate that our ZnO and ZnO:Al films grown on different temperatures are all c-axis orientation. However, the growth condition has considerable effects on the crystal structure of the films. In this section, the crystal structures of the films are investigated as a function of substrate temperature.

The crystal quality of the ZnO films prepared at various temperatures is examined. Fig. 4.1 (a) depicts the XRD spectra of the films as a function of substrate temperature. All XRD peaks are perfectly indexed and they are corresponding to ZnO wurtzite structure with predominately c-axis (002) orientation. For the film deposited at room temperature, a multiple peaks of (100), (002), (101), (102) and (110) appear in the spectrum. When the substrate temperature increases to 400 ^{o}C, the (002) peak become dominated and the other peaks are disappeared. The full width at half maximum (FWHM) of the (002) peak decreases from 0.30^{o} to 0.22^{o} when the substrate temperature increases from room temperature to 400 ^{o}C. This indicates that the grain size is enlarged with the increase of substrate temperature. With the reduction of grain size, the higher surface to volume ratio can result in more surface related defects. Hence, the ZnO films deposited at room temperature exhibit poorer crystallinity.

Cross-sectional SEM micrograph of the ZnO film prepared at the substrate temperature of 200 ^{o}C is shown in Fig. 4.1 (b). The film shows a high degree of alignment of the columnar structure, confirming the c-axis growth direction. Polly and Carter [70] reported the ZnO films deposited by combustion chemical vapor deposition. Their films deposited at 177 ^{o}C and 289 ^{o}C were amorphous with deep void within the structures. There are no amorphous phases and voids in the films prepared by the FCVA, even the films prepared at room temperature are polycrystalline and exhibit columnar structure. This is likely due to the energetic species in FCVA, which gives rise to the activation of surface diffusion and formation of dense films. Fig. 4.1 (c) depicts the AFM image of the surface morphology of the ZnO films. The scan area is 3 x 3 μm. The result shows the smooth ZnO film surface and the small grains.

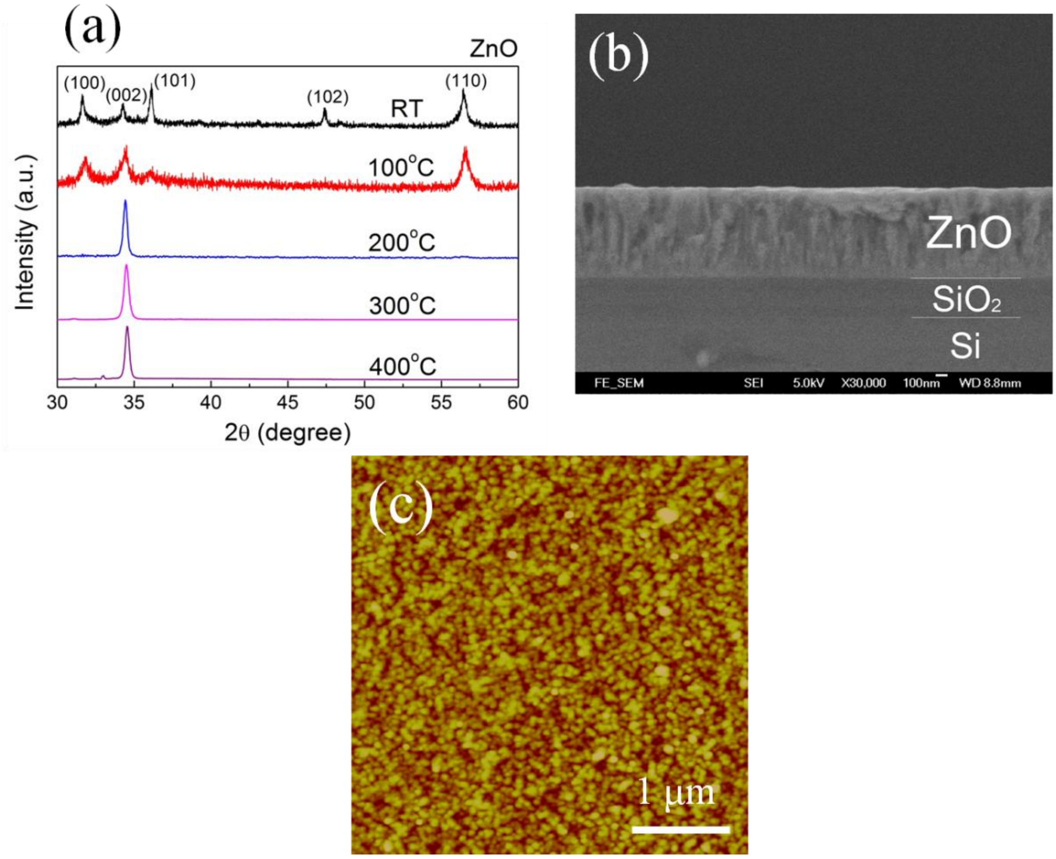

Figure 4.1 (a) XRD spectra of ZnO films prepared at different substrate temperatures. (b) Cross-sectional SEM image and (c) AFM image of the ZnO film deposited at 200 ^{o}C.

The (002) peak position (2θ $_{(002)}$) as a function of substrate temperature is plotted in Fig. 4.2. The 2θ $_{(002)}$ evidently increased from 34.26° at room temperature to 34.55° at the substrate temperature of 400 ^{o}C. Some researchers also reported the shifts of 2θ $_{(002)}$. Chen *et al.* [71] reported that the 2θ $_{(002)}$ of ZnO:Al films increased from 34.02° to 34.33° with the temperature increased from room temperature to 250 ^{o}C and then decreased to 34.43° at 350 ^{o}C. Gupta *et al.* [72] showed that the 2θ $_{(002)}$ of ZnO films increased when the temperature increased and they proposed the variation of 2θ $_{(002)}$ is due to the stresses in the films. In our experiment, we suggest the change of 2θ $_{(002)}$ and the lattice spacing d$_{(002)}$ are originated from stress within the films.

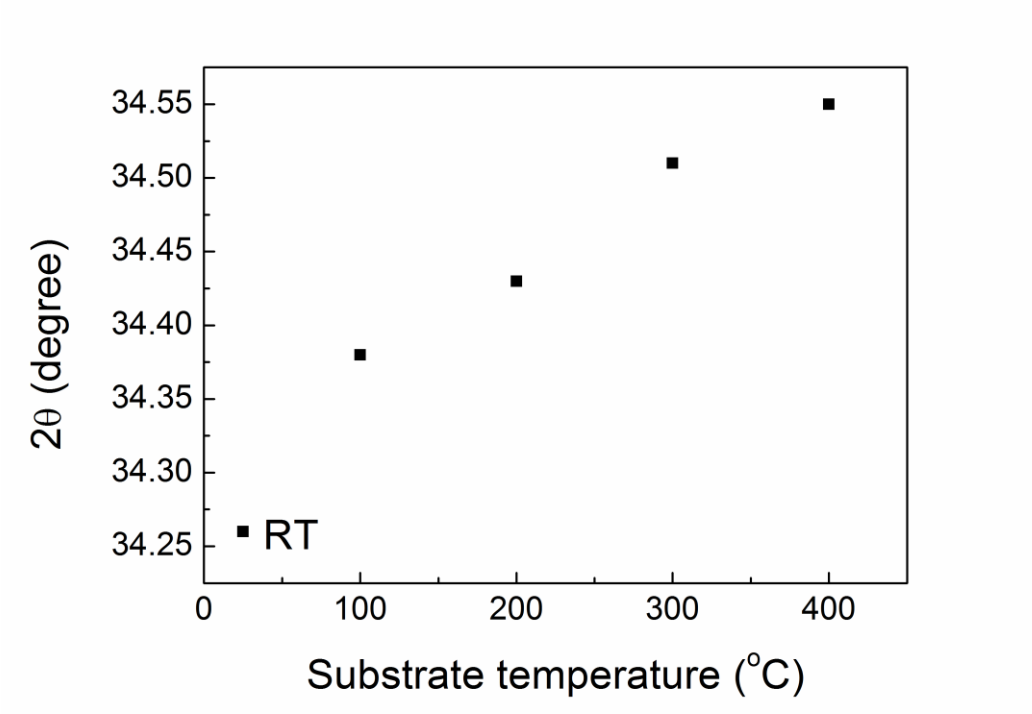

Figure 4.2 Variation of 2θ$_{(002)}$ of ZnO films against substrate temperature.

The lattice constant of the ZnO prepared at different temperatures is shown in Fig. 4.3. It is shown that the lattice constant of the ZnO film deposited at room temperature is larger as compared to the standard data of single crystalline ZnO. This indicates a compressive stress acted in the X-Y plane of the film and the unit cell was elongated along c-axis. When the substrate temperature increased, the lattice constant of c-axis also decreased and the compressive stresses became weaker.

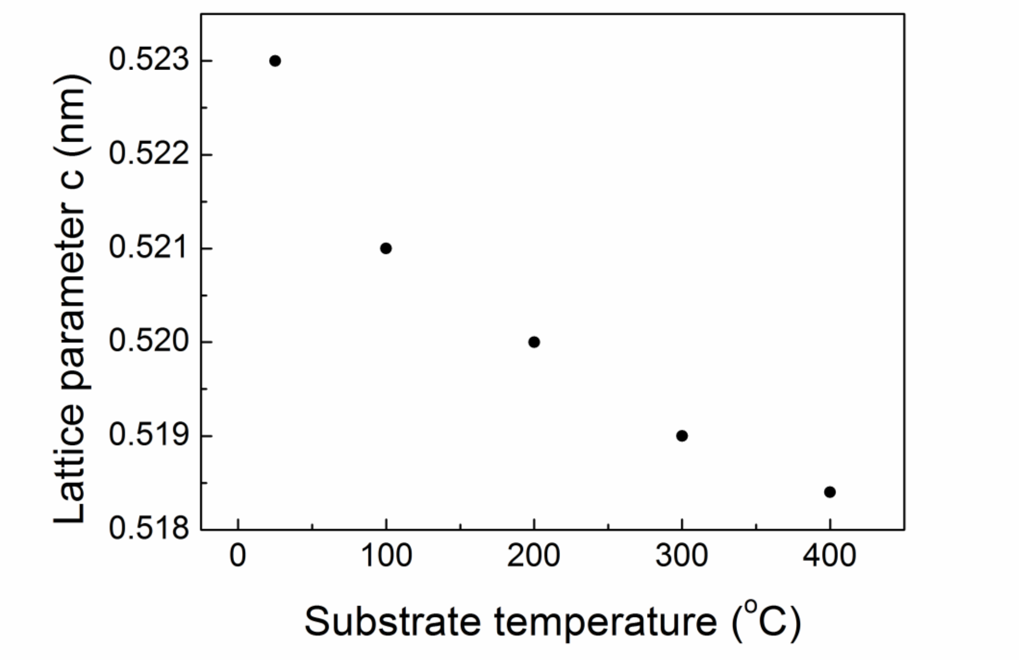

Figure 4.3 Lattice parameter of c-axis of the ZnO films against substrate temperature.

The crystallinity of the Al doped ZnO films prepared under different substrate temperatures was investigated. The film prepared at room temperature shows (100), (002) and (110) peaks from the XRD spectrum, as shown in Fig. 4.4. Similar to the ZnO, only (002) peaks was dominated at the substrate temperature of 200 ^{o}C and above. The FWHM of the (002) peak decreases from 0.32^{o} to 0.24^{o} as the substrate temperature increased to 400 ^{o}C.

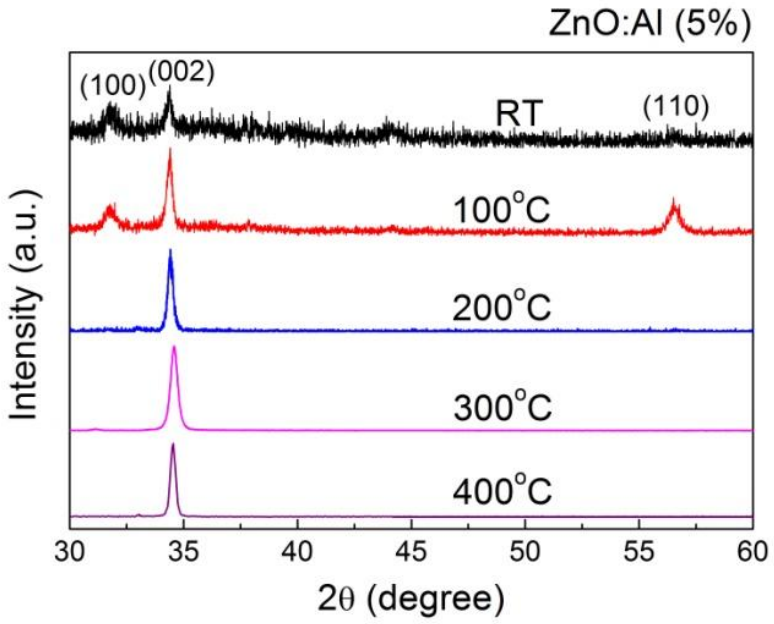

Figure 4.4 XRD spectrum of the ZnO:Al films against substrate temperature.

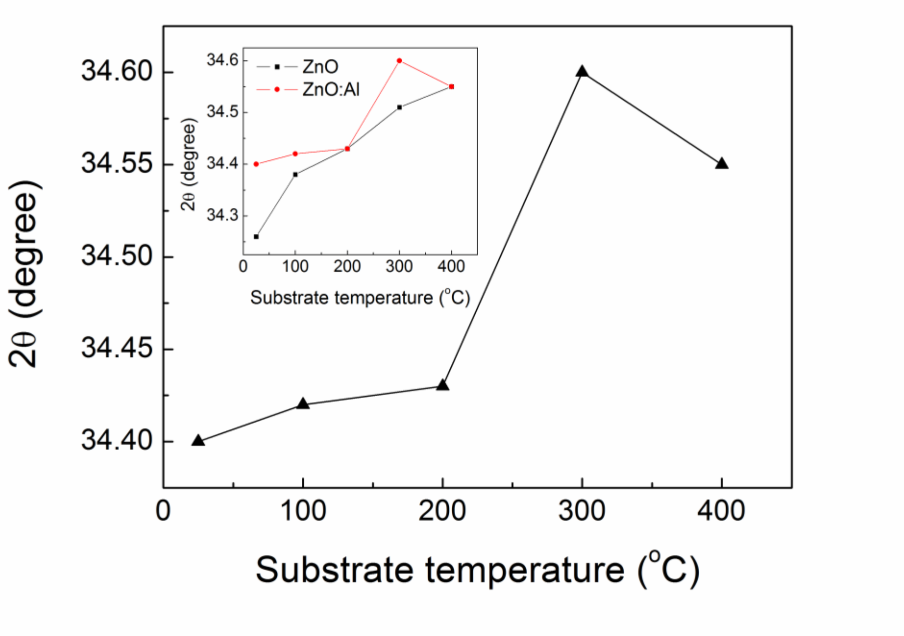

Figure 4.5 Variation of $2\theta_{(002)}$ of the ZnO:Al films against substrate temperature. The inset is a comparison of the variation of $2\theta_{(002)}$ of ZnO and ZnO:Al.

The variation of 2θ $_{(002)}$ of the ZnO:Al films against substrate temperature is shown in Fig. 4.5. The peak is shifted from 34.4^{o} to 34.6^{o} when the substrate temperature is increased from room temperature to 300 ^{o}C, and then it reduces to 34.55^{o} at 400 ^{o}C. The inset depicts a comparison of the 2θ $_{(002)}$ position of the ZnO and ZnO:Al films. With the Al doping, the peaks locate at higher diffraction angle. This observation is consistent with the results obtained by Park *et al.* [73], who observed 0.4^{o} shift to higher diffraction angle when they substituted 3 and 5 at.% Al in ZnO:Al films. They ascribed to the difference ionic radii of Zn^{2+} and Al^{3+} ions. The ionic radius of Al^{3+} is 53 pm, which is smaller than that of Zn^{2+} (72 pm). The substitution replacement of Al ions leads to higher diffraction angle and the lattice parameter of c-axis is expected to be shorter. However, Xu *et al*. [74] observed a reverse shift as the (002) peak position changed to lower value as compared to their ZnO thin films. They concluded that the films were in a uniform state of stress with a tensile component parallel to c-axis.

The lattice parameter c of the ZnO:Al films grown at different substrate temperatures is shown in Fig. 4.6. The lattice constant c decreases when the substrate temperature increases. Comparing with the result of the ZnO, the lattice parameter c of the ZnO:Al appears shorter even at 200 ^{o}C and 400 ^{o}C the c-axis of the ZnO:Al is fragmentally longer than ZnO. It indicates that Al ions substitute into Zn-O sites and cause a reduction of c-axis.

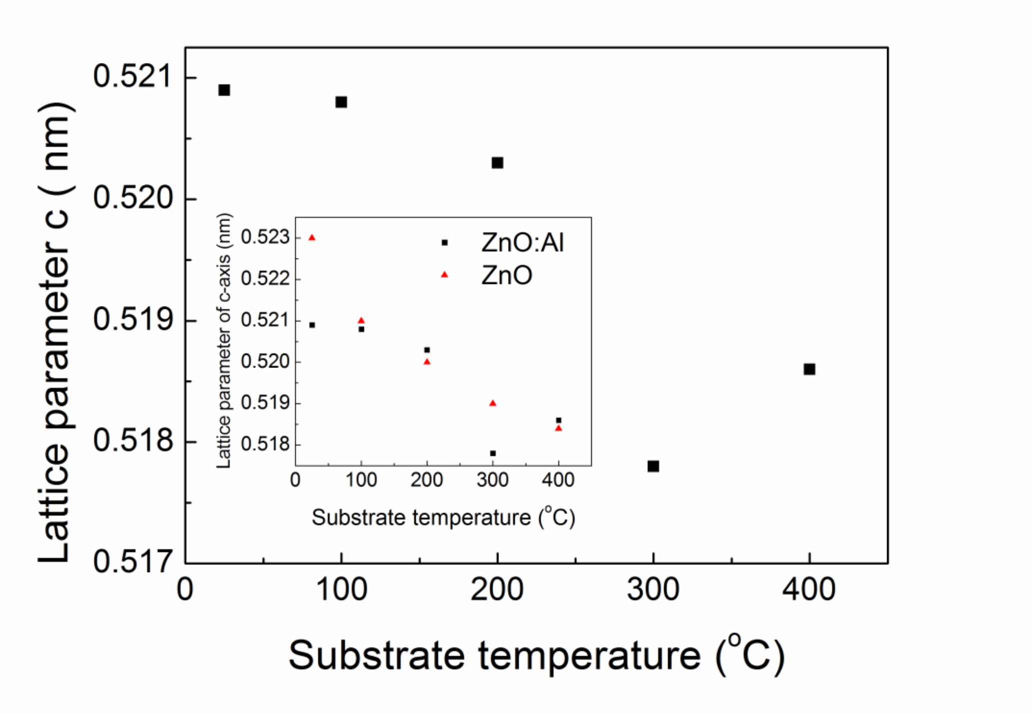

Figure 4.6 Lattice parameter of c-axis of the ZnO:Al against substrate temperature. The inset is a comparison of the lattice parameter of ZnO and ZnO:Al.

4.1.2 Electrical measurement

All the transparent ZnO and ZnO:Al films exhibited n-type conductivity. The high conductivity of the films mainly results from the stoichiometric deviation [71]. Generally, the conduction electrons are supplied from donor sites associated with oxygen vacancies or zinc interstitial. These donor sites can be easily obtained by chemical reduction or intentional doping. For ZnO films, the conduction characteristic is dominated by electrons generated from O^{2-} vacancies or Zn interstitial atoms [73]. The electrical conduction of the ZnO:Al films is attributed to Al^{3+} ions on substitution sites of Zn^{2+} ions and Al interstitial atoms in addition to oxygen vacancies and zinc interstitial atoms. The electrical conductivity can be influenced by the growth condition, in particular the substrate temperature and oxygen pressure.

The resistivity, carrier concentration and Hall mobility of the ZnO films prepared at different temperatures is shown in Fig. 4.7. The carrier concentration increases about one order of magnitude when the substrate temperature increases from room temperature to 400 ^{o}C. Park et al. [73] attributed the variation of carrier concentration with substrate temperature to the different amount of oxygen vacancies within the films. In our FCVA system, the distance between the substrate holder and the oxygen outlet is quite long (~ 25 cm). The oxygen gas completely reacts with zinc plasma and it will form ZnO before reaching the substrate. The amount of oxygen nearby the substrate will therefore decrease. The reduced oxygen atmosphere helps oxygen outdiffusion at higher temperature, leading to decrease of amount of oxygen content in the films. Hence, the oxygen deficient drastically increases the number of interstitial zinc atoms and oxygen vacancies and in turn the carrier concentration.

The variation of Hall mobility with the substrate temperatures can be explained in terms of two scattering mechanism: free carrier scattering and grain boundary scattering. The free carrier scattering is dominated when the Hall mobility decreases with the increase of carrier concentration. On the other hand, when the Hall mobility increases with the increase of carrier concentration, the grain boundary scattering governs. As shown in Fig. 4.7, the Hall mobility and carrier concentration continuously increases with the substrate temperature. Hence, we can conclude that the grain boundary scattering dominates for the free carrier transport. The resistivity of the ZnO films reduces when the substrate temperature increases.

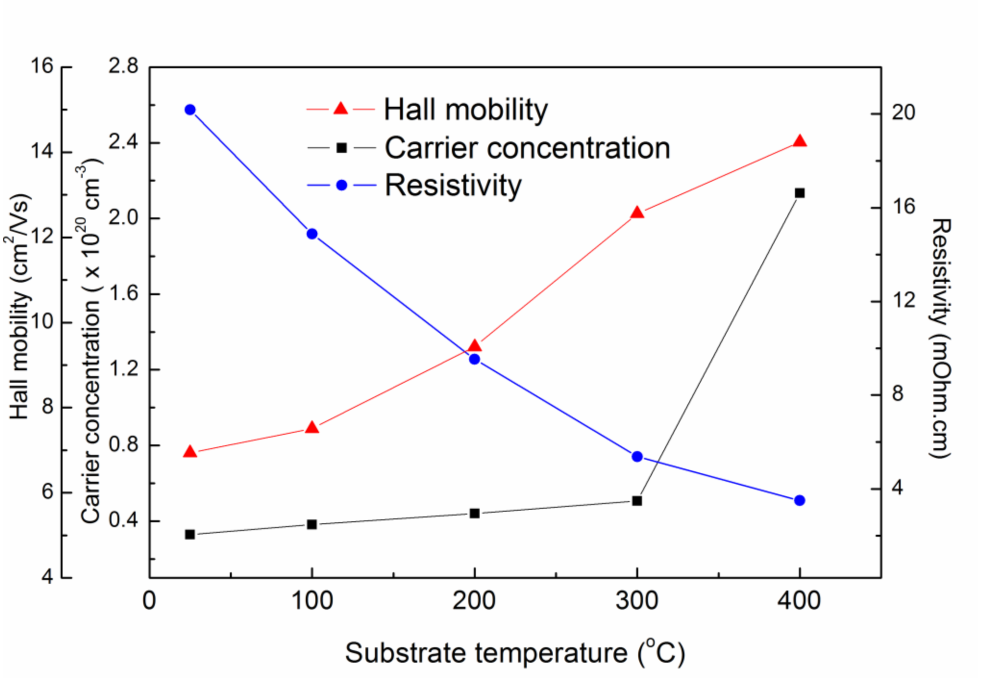

Figure 4.7 Carrier concentration, Hall mobility and resistivity of the ZnO films as a function of substrate temperature.

The carrier concentration, Hall mobility and resistivity of the ZnO:Al films with the substrate temperatures is shown in Fig. 4.8. It is shown that the carrier concentration with the Al doping is higher than the undoped ZnO. This increase may come from the donor concentration increase resulting from the Al doping. The Hall mobility of the ZnO:Al films has a similar trend to the undoped ZnO, while the Al doping enhances the Hall mobility of the films. The resistivity of the ZnO:Al films is lower than that of the ZnO films because of the contribution from Al^{3+} ions on substitutional sites of Zn^{2+} ions and Al interstitial atoms.

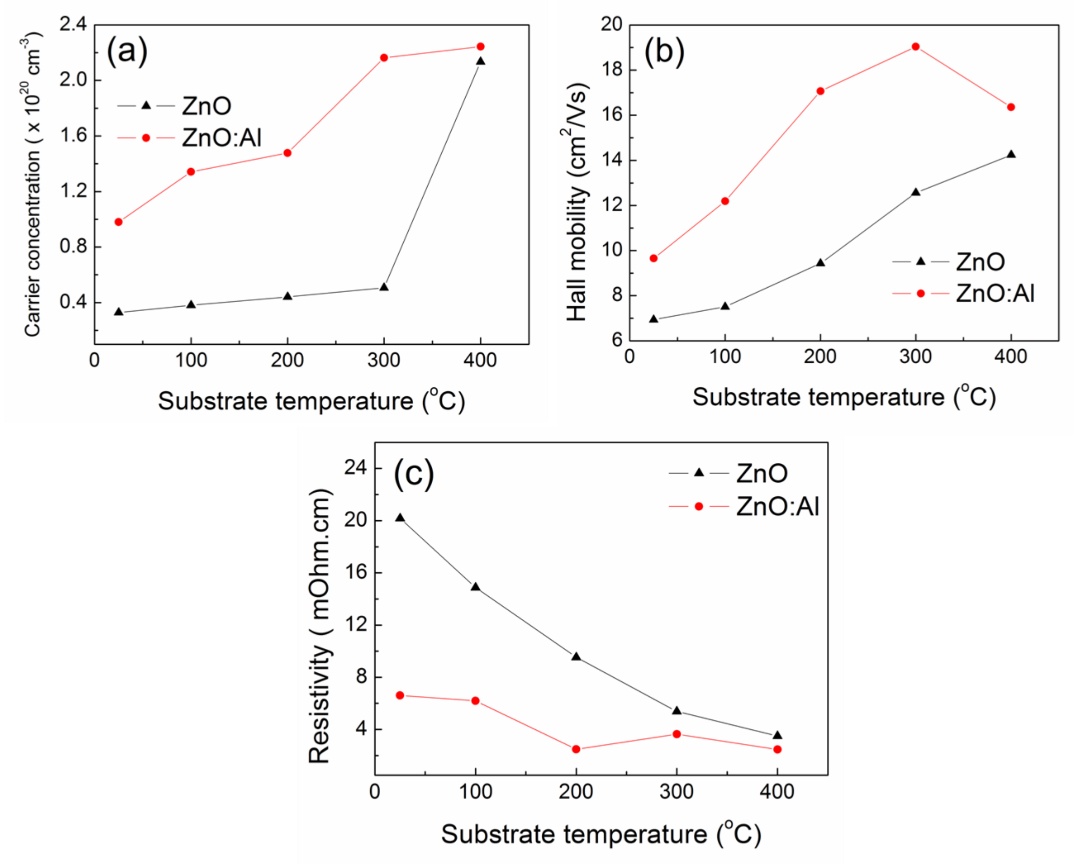

Figure 4.8 (a) Carrier concentration, (b) Hall mobility and (c) resistivity of the ZnO and ZnO:Al films against substrate temperatures.

4.1.3 Optical measurement

4.1.3.1 Transmittance

Fig. 4.9 (a) shows the dependence of transmittance of the ZnO films prepared at various substrate temperatures. For all the films, a high transmittance of about 90% was obtained in the visible wavelength regions. The oscillations in the spectrum are caused by optical interference on the smooth surface. A steep falloff is observed at around 370 nm for all the films, which is a characteristic of high crystal quality film. High transmittance is also observed for the ZnO:Al films, as shown in Fig. 4.9 (b).

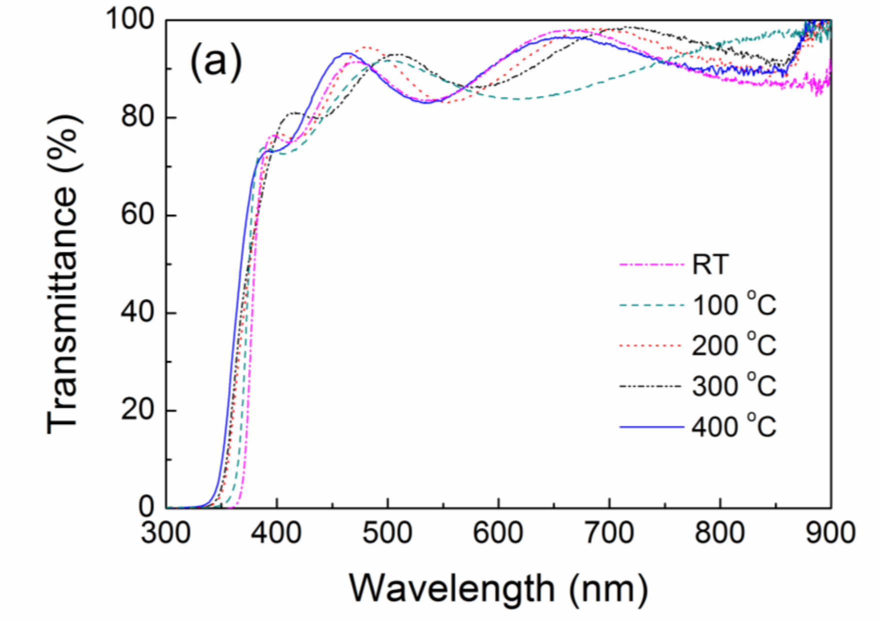

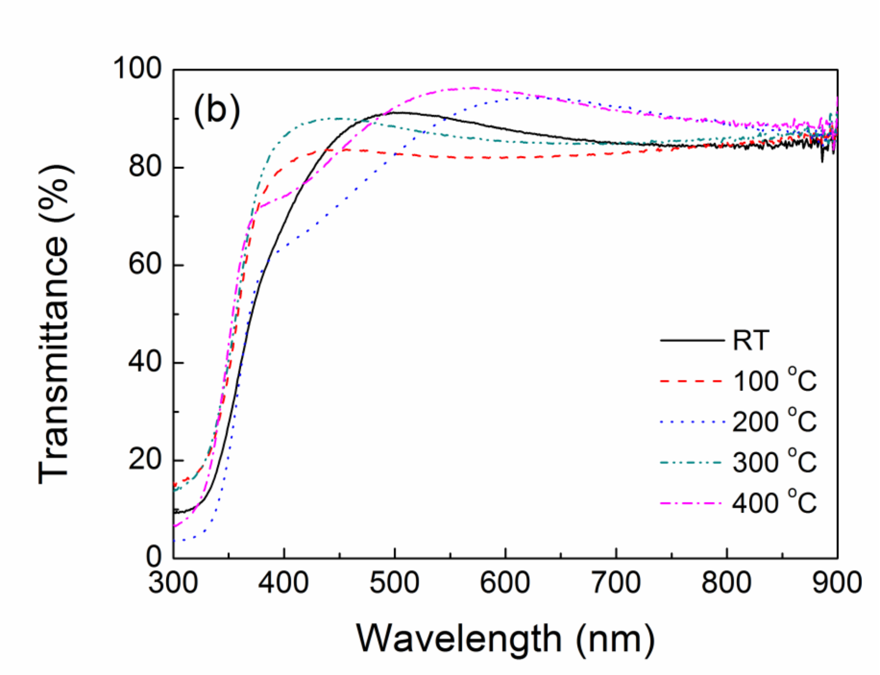

Figure 4.9 Optical transmittance spectrum of the (a) ZnO and (b) ZnO:Al films prepared at various substrate temperatures.

4.1.3.2 Photoluminescence

The room temperature PL spectra of the ZnO films are plotted in Fig. 4.10. The PL shows a sharp near band edge emission at the wavelength of ~ 375 nm, which is dominated by free exciton recombination. There is a broad deep level emission band at ~ 520 nm when the substrate temperature increases to 300°C and above. Nevertheless, the high intensity ratio of near band edge emission to deep level emission indicates that the ZnO films have high crystal quality. In addition, the high carrier concentration in our films may help improve the excitonic luminescence by passivating deep defect level and non-radiative centers [75]. As the substrate temperature increases, the peak position of the excitonic emission shifts from 372 to 379 nm and it implies that the band gap narrowing effect occurred as the substrate temperature increases. Moreover, a broader emission peak is observed at the temperature of 300 °C and above. It is thought that the red shift of the UV peak emission is caused by the microstructural change in crystal and some surface states, defect and dangling bonds could be considered as the causes of the band tail. [76]

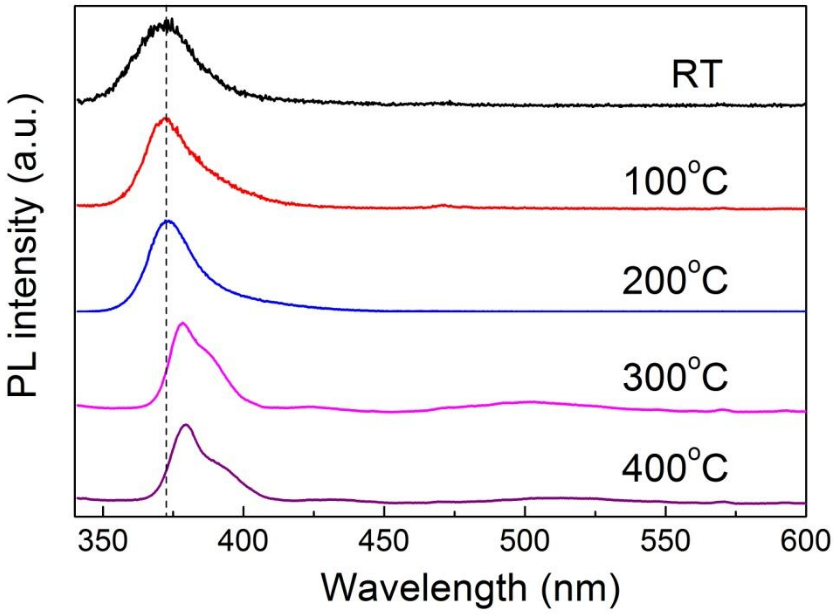

Figure 4.10 Room temperature PL spectra of the ZnO films deposited at different substrate temperatures.

Fig. 4.11 shows the room temperature PL of the ZnO:Al films. The spectra were measured at the same condition as the ZnO films. As shown in the spectra, the ZnO:Al films illustrate a UV peak at ~ 365 nm, which is shorter than those from ZnO films. The results agree well with the observation from the optical transmittance measurements. The PL spectra of all the ZnO:Al films exist an emission band tail extend to ~ 420 nm. The emission band tail of the ZnO:Al films may be due to the conduction band tail which usually occurred in heavily doped semiconductor [77].

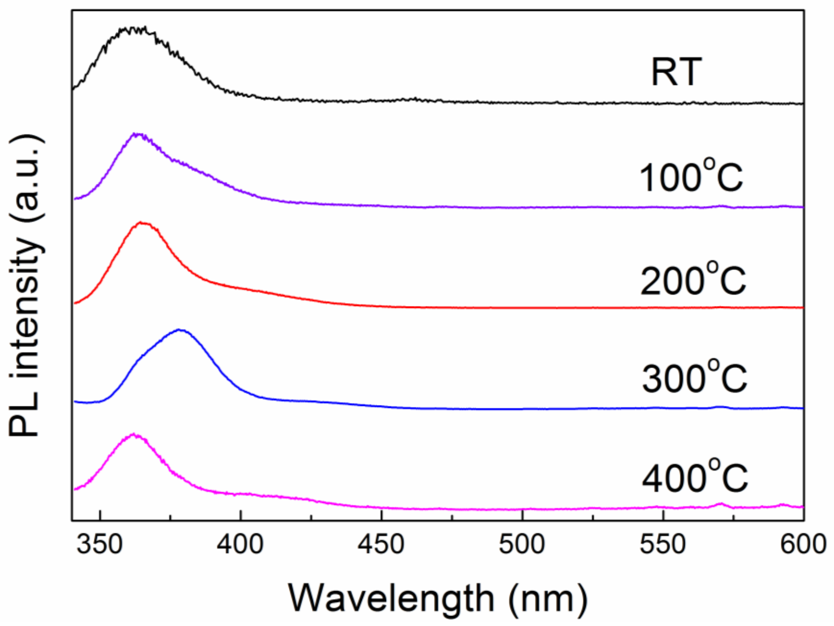

Figure 4.11 Room temperature PL spectra of the ZnO:Al films deposited at different substrate temperatures.

4.2 Effects of doping concentration

4.2.1 Electrical properties

Fig. 4.12 shows the plot of the carrier concentration, Hall mobility and resistivity of the ZnO:Al films prepared with ZnAl targets of various Al contents. The films were deposited at the substrate temperature of 200 °C. The carrier concentration increases with increasing Al content, leading to the reduction of the resistivity. As a result, the Hall mobility increases with the Al content. It is believed that the increase of the carrier concentration comes from the ionization of the Al into Al^{3+} and replacement with Zn^{2+}. Hence, more free electrons are produced from the zinc atoms replacement.

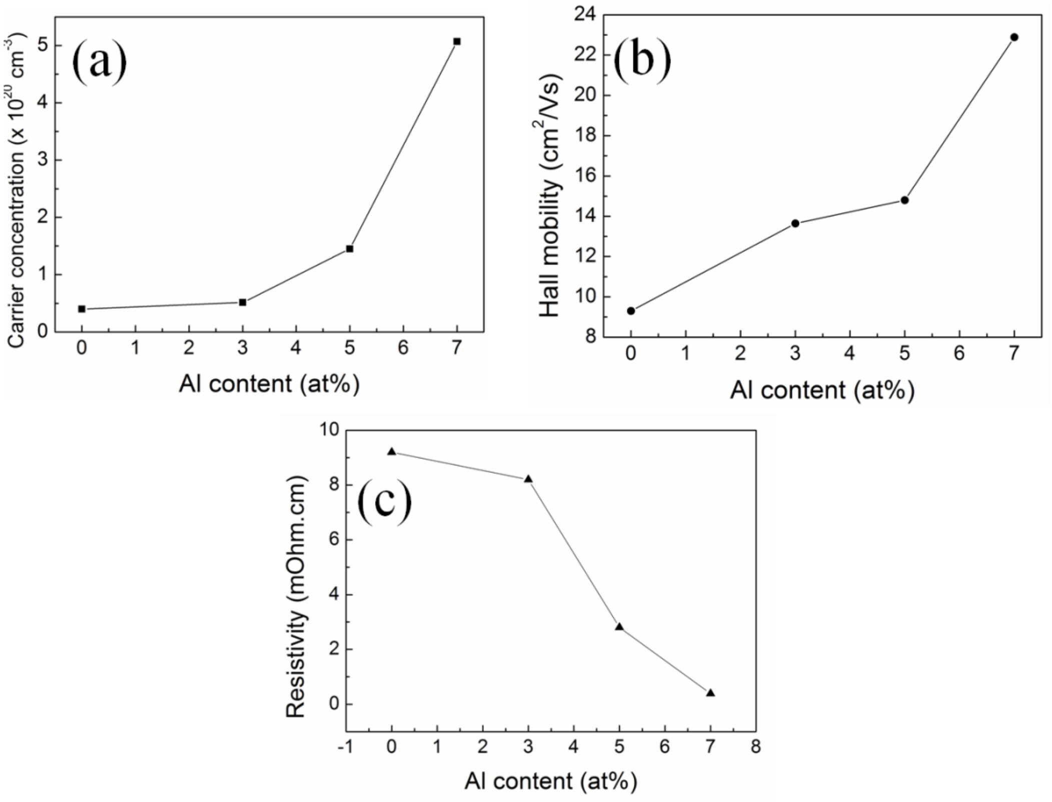

Figure 4.12 (a) Carrier concentration, (b) Hall mobility and (c) resistivity as a function of Al content.

4.2.2 Transmittance

Fig. 4.13 (a) shows the transmittance spectra of the ZnO:Al films with various Al contents. The overall transmittance of the films is ~ 90%, indicating that the high transmittance is not affected by Al doping. It is observed that the falloff in the transmittance spectra is shifted toward shorter wavelength region when increasing the Al doping. The blueshift of the absorption edge of ZnO:Al films is associated with the Burstein-Moss effect. Using the transmittance data near the absorption edge, the energy band gap can be estimated by plotting the square of absorption coefficient as a function of photon energy, as shown in Fig. 4.13 (b). The transformation from transmittance to absorption coefficient is described in Chapter 3. Doping the ZnO with Al increases the energy band gap from 3.38 to 3.53 eV.

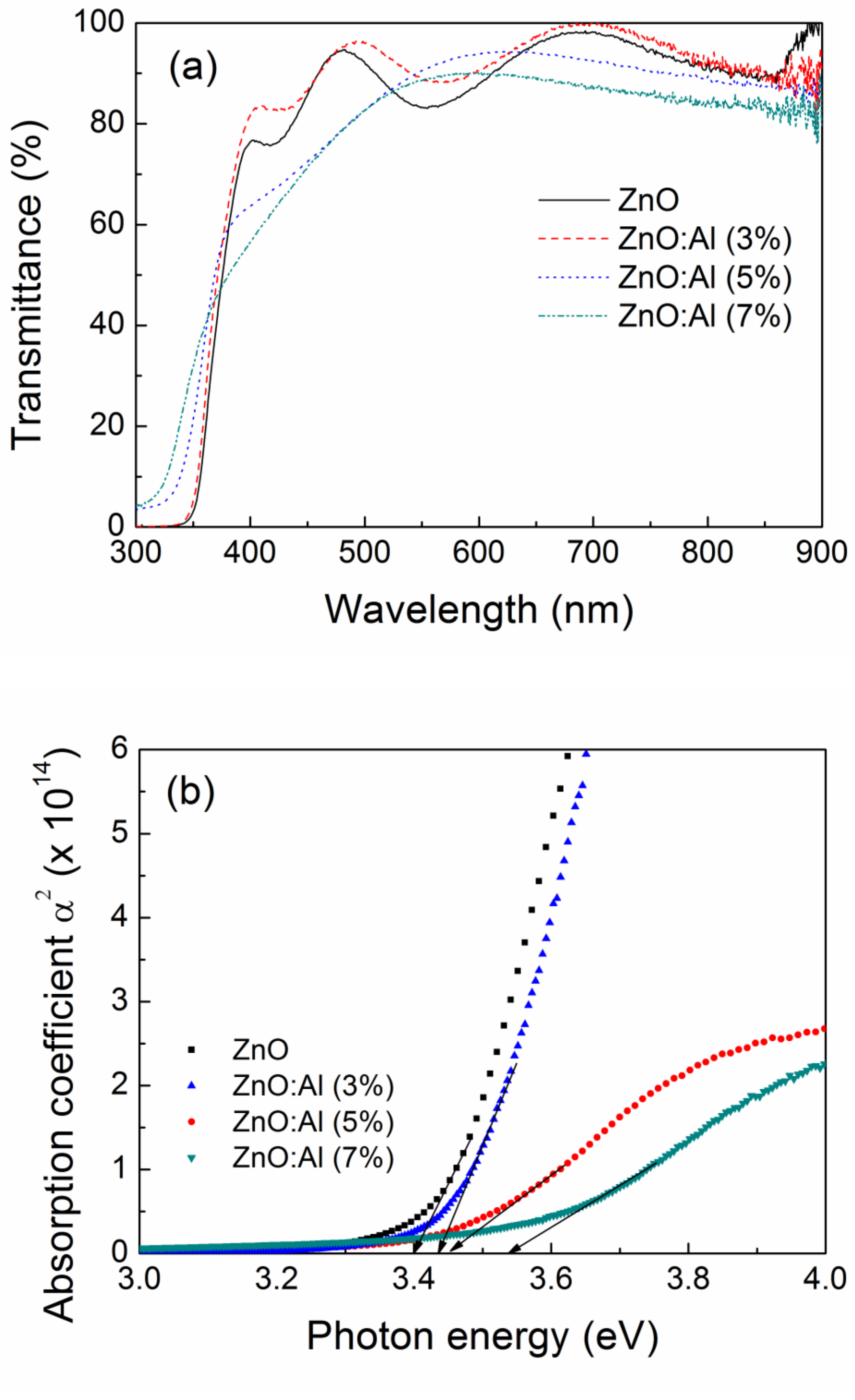

Figure 4.13 (a) Transmittance of the ZnO:Al films with various Al contents and (b) square of the absorption coefficient as a function of photon energy for the ZnO:Al films.

4.2.3 Photoluminescence

The dependence of the PL emission on Al doping concentration is also studied. As shown in Fig. 4.14, the peak of near bad edge emission of the films has a blue shift to shorter wavelength as the Al doping concentration increases. For the pure ZnO, the near band edge emission is located at around 375 nm. It then shifts to ~360 nm as the Al doping concentration increases to 7 at%. It is believed to be Burstein-Moss shift due to the doping of Al in the ZnO films.

It is also observed that the PL bands are broadened with increasing Al doping concentration. It is probably that defect states may be created when the ZnO films are doped with Al, allowing for the electron hole recombination through the defect states.

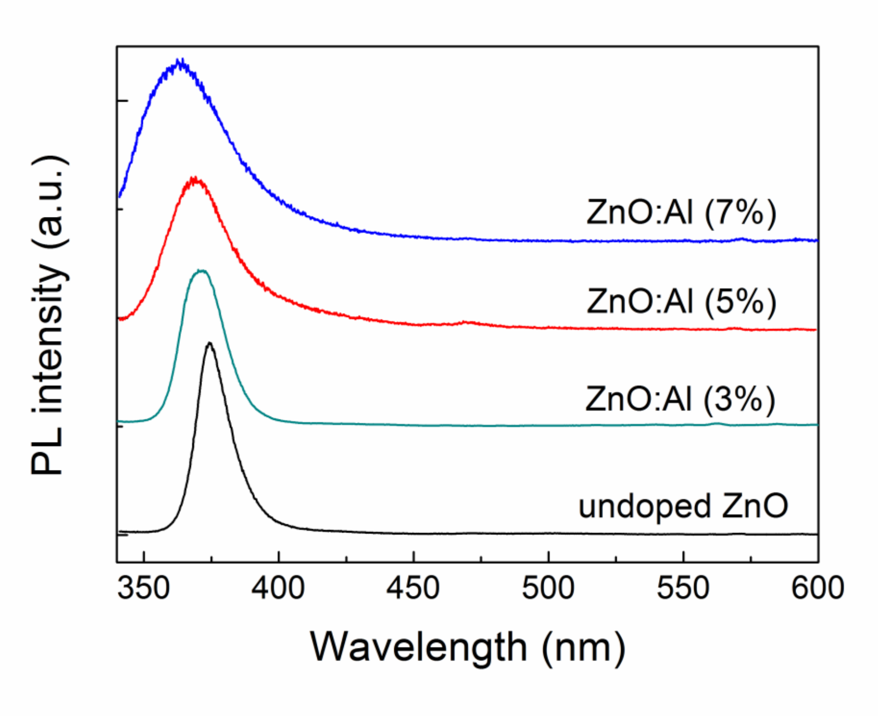

Figure 4.14 Room temperature PL spectra of undoped ZnO, ZnO (3 at%), ZnO:Al (5 at%) and ZnO:Al (7 at%).

4.3 Summary

The undoped and Al doped ZnO thin films were deposited at different substrate temperatures on SiO_2/Si substrate by the FCVA technique. The structural investigation shows that all the films exhibit c-axis orientation. The carrier concentration and Hall mobility of the films increase with the substrate temperature. As for the optical properties, both the ZnO and ZnO:Al films have a high transmittance of ~ 85% in the visible region. The PL results of the ZnO exhibits a UV emission at ~ 375 nm. For the ZnO:Al films, a shorter emission wavelength is observed which indicates the broadening of the energy band gap. Doping the ZnO with Al enhances the electrical conductivity and causes the PL band as well as the bandgap broadening.

Chapter 5 Fabrication and characterization of heterojunction light-emitting diodes

5.1 Introduction

In the previous chapter, we have studied the properties of the ZnO and ZnO:Al films. A strong UV emission was obtained from all the films. Therefore, ZnO-based LEDs can be fabricated. Although the ZnO-based *p*-*n* homojunction LEDs have been demonstrated [78], the reproducible and reliable production of *p*-type ZnO films with high carrier concentration and hole mobility remain a challenge. In order to avoid *p*-type doping of ZnO, heterojunction LEDs have been fabricated by growing ZnO films onto *p*-type material. A number of groups have employed *p*-Si to fabricate *n*-ZnO/*p*-Si heterojunction LEDs due to the low-cost fabrication. [79,80]. However, the reported EL emissions were observed in the broad visible range due to defect-related deep level emission. Meanwhile, *p*-GaN or *p*-AlGaN have been widely used because of their similar physical properties and small lattice mismatch (~ 1.8%) with ZnO. Some researchers have fabricated *n*-ZnO/*p*-GaN heterojunction LEDs by various techniques such as radio frequency (rf) sputtering [81] and molecular beam epitaxy (MBE) [82]. However, the emissions from these ZnO/GaN LEDs are usually weak because of the formation of nonradiative center at the interface. It is desirable to use low-temperature grown ZnO films prepared by vacuum arc deposition for ZnO based LEDs. This is because such technique is characterized by high ion energy and high kinetic energy of growing precursors, which play an important role in the realization of low temperature deposition [16], as described in Chapter 2. In this chapter, we fabricate *n*-ZnO:Al/*i*-ZnO/*p*-GaN heterojunction LED, utilizing the films prepared at low deposition temperature. It is shown that the ZnO film has high crystal quality and the heterojunction LED exhibits UV emission peak at room temperature.

5.2 Fabrication

A 300 nm of ZnO film were deposited on GaN:Mg/Al_2O_3 by the FCVA technique. The apparatus of the FCVA system is described in Chapter 3. During the deposition, the substrate temperature was set at 200℃ and the oxygen pressure was kept at 2 mTorr. The advantage of using such temperature is that this temperature can grow the films with good optical properties. A ZnO:Al (7%) layer of thickness of 200 nm was deposited on ITO glass by the FCVA technique with the same deposition conditions as the ZnO film. A Zn target with 7 at% of Al was employed in this deposition process. Because of its lower resistivity ($< 5 \times 10^{-4}$ Ωcm), higher carrier concentration ($> 1 \times 10^{20}$ cm^{-3}) and wider bandgap (~ 0.15 eV), the ZnO:Al (7%) acts as a transparent electrons injector. Fig. 5.1 shows the schematic diagram of the heterojunction LED. The electrical and optical characteristics of the *n*-ZnO:Al/*i*-ZnO/*p*-GaN:Mg heterojunction LED were measured by vertical contact approach, at which contacting the *n* side of the LED to the ZnO:Al (7%)-deposited ITO glass. This configuration is able to avoid metallization on the ZnO:Al (7%) of the LED, suggesting that the fabrication process can be simplified and the device can be recycled for other processes [83].

Finally, Ohmic contact to the ZnO:Al films and GaN:Mg were made by applying ITO layer and indium film respectively.

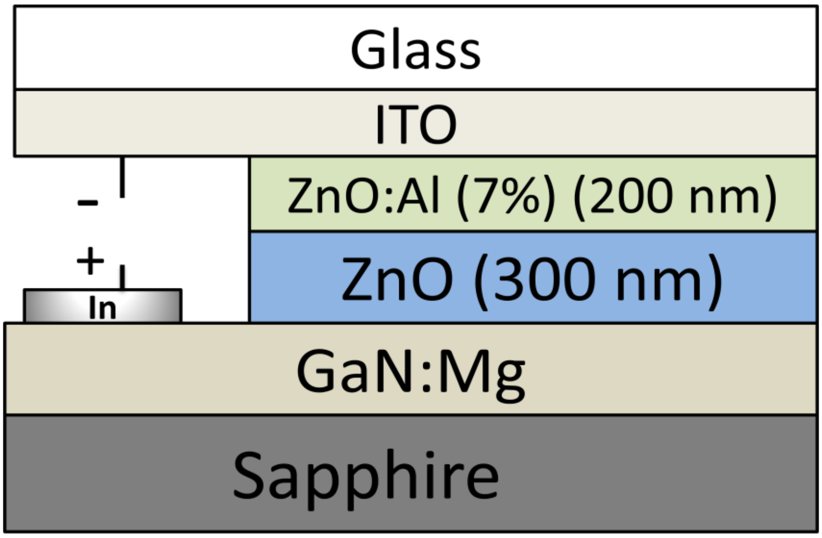

Figure 5.1 Schematic diagram of the heterojunction.

5.3 Current-voltage characteristics

Fig. 5.2 shows the room temperature current-voltage (I-V) characteristics of the heterojunction LEDs. The device shows nonlinear rectifying behavior. The I-V characteristics of the ZnO:Al/ITO and GaN:Mg/In contact are shown in the inset of Fig. 5.2. The GaN:Mg/In contact shows a fairly linear I-V curve, while the ZnO:Al/ITO exhibits a excellent linear characteristics. This indicates that the rectifying diode-like behavior is originated from ZnO/GaN:Mg heterojunction. The ideality factor *n* can be calculated from Shockley's Law [84]:

$$I = I_S[\exp\left(\frac{qV}{nkT}\right) - 1] \qquad (1)$$

where I_S is saturation current, q is the electrical charge, k is Boltzmann constant and T is the temperature (=300 K). n is calculated to be approximately 4 for the device. It can be seen from these data that the I-V characteristics of the structure are comparable to the previous works [61, 85].

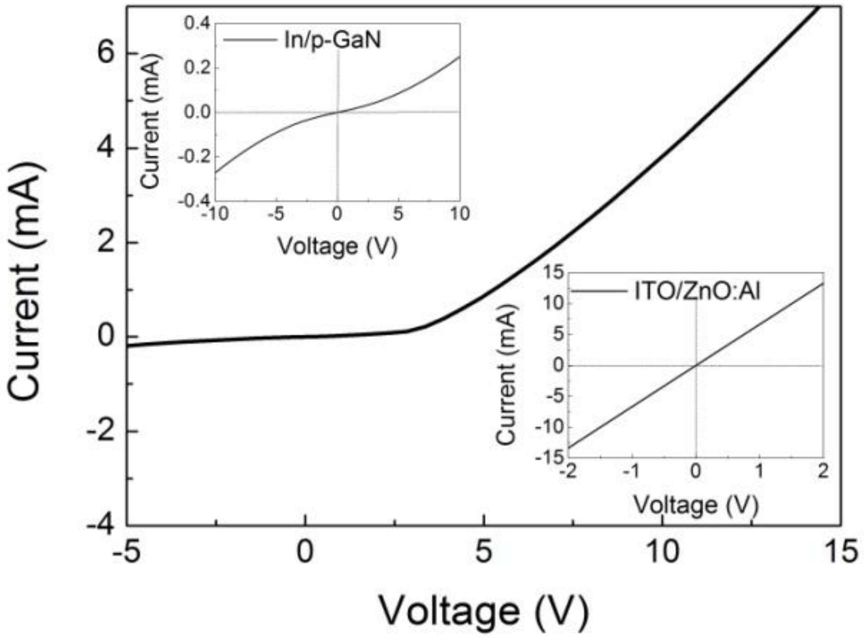

Figure 5.2 I-V characteristics of the heterojunction. The insets show n- and p-type ohmic contacts.

5.4 Electroluminescence

The EL spectra of the heterojunction LEDs under various forward-bias voltages are shown in Fig. 5.3. It is observed that the device is dominated by UV emission peaked at around 370 nm with a long tail extending to around 470 nm at various bias voltages. It should be noted that no emission is observed at the reverse bias. The FWHM of the LEDs is about 9 nm. Although a number of research have reported UV EL emission of LEDs, the reported FWHMs of the EL peaks are usually quite large, which are ranged from ~ 17 to 180 nm [79, 86-88].

By enlarging the UV regime in the EL spectra, it is seen that the EL spectra consist of two components, as shown in Fig. 5.3 (b). The Gaussian fittings were conducted and the curves depict that there are two emission peaks which are dominated at ~ 369 nm and ~ 377 nm. In order to understand the origin of the UV emission, the PL spectra of the ZnO:Al (7%), ZnO and GaN:Mg films were carried out. Fig. 5.4 shows the PL spectra of the corresponding layers. The PL of the ZnO is peaked at around 375 nm, while that of the ZnO:Al (7%) is at ~ 364 nm. For the GaN:Mg films, the PL spectrum contains a strong blue emission band at ~ 440 nm associated with the transition from the conduction band to the Mg acceptor level [89], and a weak UV emission at ~ 378 nm. By the comparison of the PL and EL spectra, the Gaussian peak at ~ 369 nm is likely to be attributed to the ZnO:Al films, whereas the ~ 377 nm peak is emerged from the ZnO films. On the other hand, the UV emission might not be originated from the GaN:Mg because the UV emission from the PL is relatively weak. Hence, it is believed that the EL emission is emerged from the ZnO and ZnO:Al (7%).

In addition, the light-voltage curve is depicted in Fig. 5.5. The turn-on voltage is around 7 V. Large turn-on voltage might be attributed to high Ohmic contact resistance and interface defect between ZnO:Al (7%) and ZnO or ZnO and GaN:Mg.

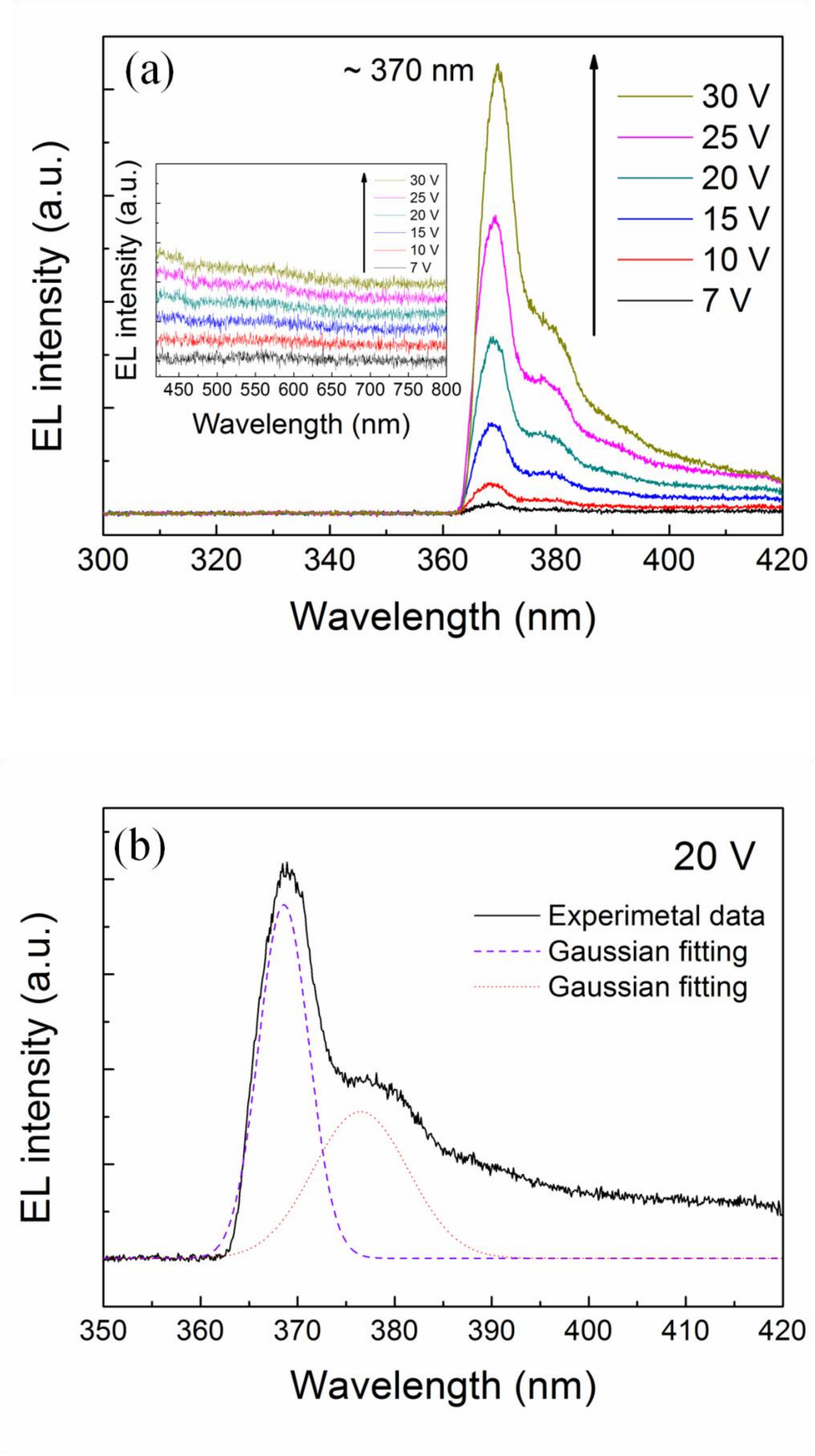

Figure 5.3 (a) EL spectra under various bias voltage and (b) Gaussian fitting of the EL spectrum obtained at 20 V.

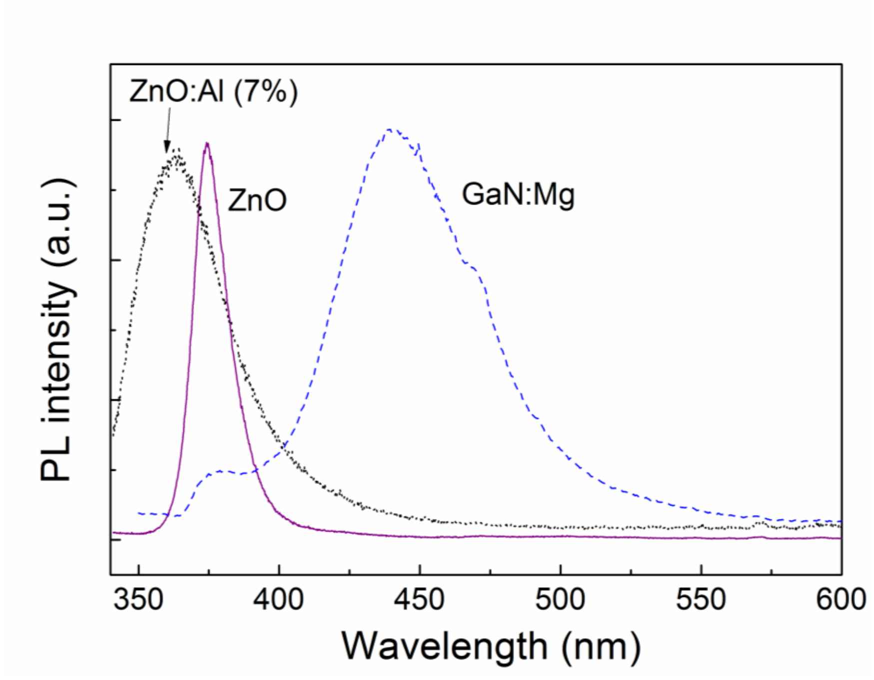

Figure 5.4 PL spectra of the ZnO, ZnO:Al (7%) and GaN:Mg films.

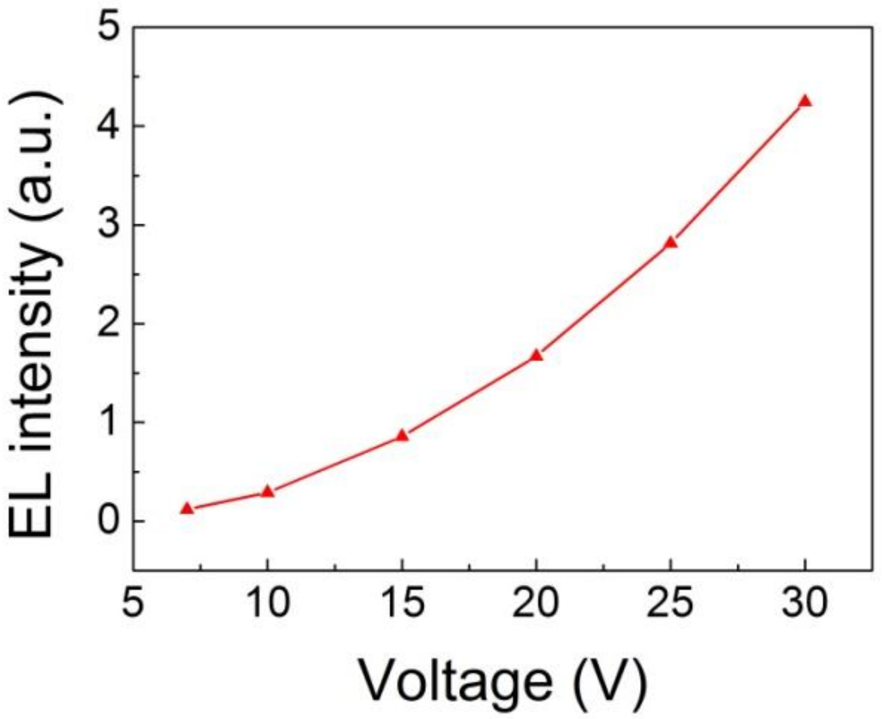

Figure 5.5 EL intensity as a function of the biased voltages.

The UV EL mechanism can be explained by using energy band structure of the heterojunction devices. The band diagram of the *n*-ZnO/*i*-ZnO/*p*-GaN:Mg heterostructure is drawn using Anderson Model, as shown in Fig. 5.6. The bandgap energy for ZnO is assumed as about 3.3 eV and 3.51 eV for GaN:Mg. The electron affinity (χ) for ZnO and GaN:Mg is about 4.35 and 3.9 eV respectively. From the diagram, the energetic barrier for electrons is $\Delta E_C = \chi_{(ZnO)} - \chi_{(GaN:Mg)} = 4.35 - 3.9 = 0.45$ eV, while the holes barrier $\Delta E_V = E_{g(ZnO)} + \Delta E_C - E_{g(GaN:Mg)} = 3.3 + 0.45 - 3.51 = 0.24$ eV. It is shown that the electrons barrier is much higher than holes barrier, inferring that the holes can drift from GaN:Mg to ZnO through the barrier and the recombination takes place in the ZnO region.

Moreover, the observation of the two UV emission peaks from the ZnO:Al (7%) and ZnO films might be due to the radiative recombination at the interface between the two films. The electron flow in the ZnO and ZnO:Al (7%) are relative large, compared with the hole injection of GaN:Mg. The use of the vertical contact geometry can reduce the electron injection from the ZnO:Al (7%). Enhanced hole injection from the GaN:Mg to ZnO and ZnO:Al (7%) could compensates for the electron-hole injection asymmetry caused by the large difference of the carrier concentrations.

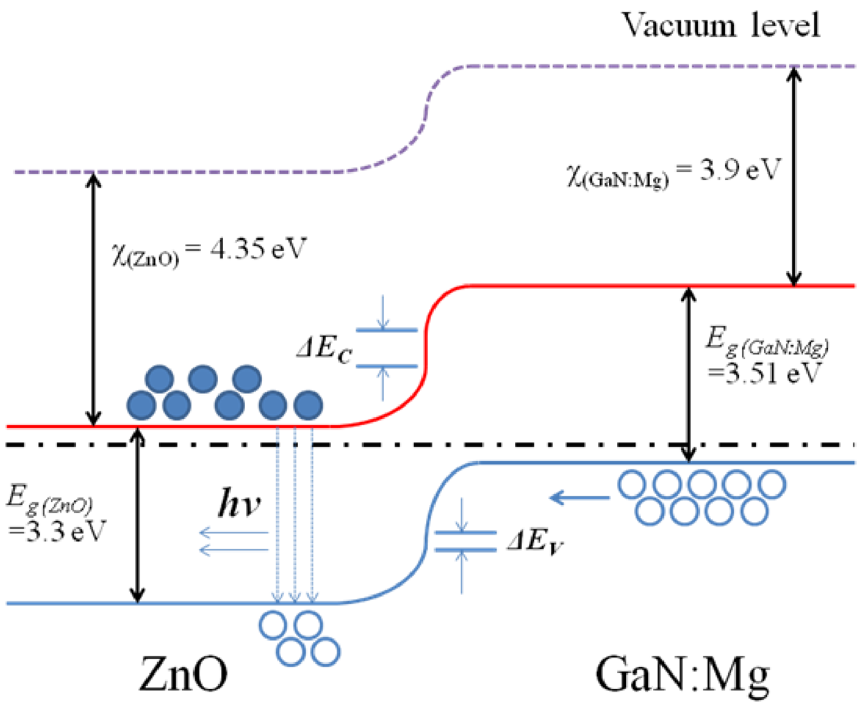

Figure 5.6 Energy band diagram of the heterojunction.

5.5 Summary

The n-ZnO:Al/i-ZnO/p-GaN:Mg heterojunction LEDs have been fabricated. The structure shows a nonlinear rectifying behavior. The LEDs exhibited room temperature EL, showing the UV emission band. The UV band is attributed to the radiative recombination within the ZnO:Al (7%) and ZnO films because of the compensation for the difference of carrier concentrations by vertical contact approach.

Chapter 6 Synthesis of ZnO nanorods and their optoelectronic properties

6.1 Introduction

In the last few chapters, we have considered the fabrication and characterization of the ZnO thin films. Indeed, the ZnO-based nanostructures for optoelectronic applications have attracted much attention. Over the past few years, various ZnO one-dimensional nanostructures including nanowires [90], nanorods [91, 92], nanobelts [93, 94] and nanotubes [95] have been synthesized by different approaches. The approaches include metal-organic chemical vapor deposition (MOCVD) [96], CVD [97], thermal evaporation [94], pulsed laser deposition (PLD) [98], solution method [99] and template-based growth technique [100].

The solution method has been widely used to synthesize ZnO nanowires and nanorods due to its simplicity, low cost and fewer apparatuses. In this chapter, fabrication and characterization of ZnO nanorods via low-temperature chemical aqueous method were carried out. In order to utilize the as-grown nanorods, hybrids LEDs were fabricated with the organic semiconductor. The origin of emission of the LEDs will be studied.

6.2 Experimental

The ZnO nanorods were grown on the SiO_2/Si substrate. Before the growth of nanorods, the substrates were cleaned by acetone and isopropyl alcohol in ultrasound bath for 15 minutes respectively, and then were dried in air. A ZnO buffer layer with the thickness of ~ 20 nm was deposited on the substrates by the

FCVA technique, as described in Chapter 3. The substrate temperature was adjusted from room temperature to 400 ^oC. The oxygen flow rate was kept constant at 40 SCCM.

In order to prepare the mixture, 2.97 grams of zinc nitrate hexahydrate ($Zn(NO_3)_2 \cdot 6H_2O$) powder and 1.42 grams of hexamethyl tetramine ($C_6H_{12}N_4$) were added to deionized water so that the 0.1 M of $Zn(NO_3)_2 \cdot 6H_2O$ and 0.1 M of $C_6H_{12}N_4$ mixtures were obtained. Subsequently, the two mixtures were added together. Fig. 6.1 shows the setup for the growth of the ZnO nanorods. The substrates were placed into the solution and heated at the temperature of 95 ^oC. The growth time of the ZnO nanorods is 1 hour. The samples were taken away from the solution and rinsed by deionized water in order to wash away the ZnO clusters.

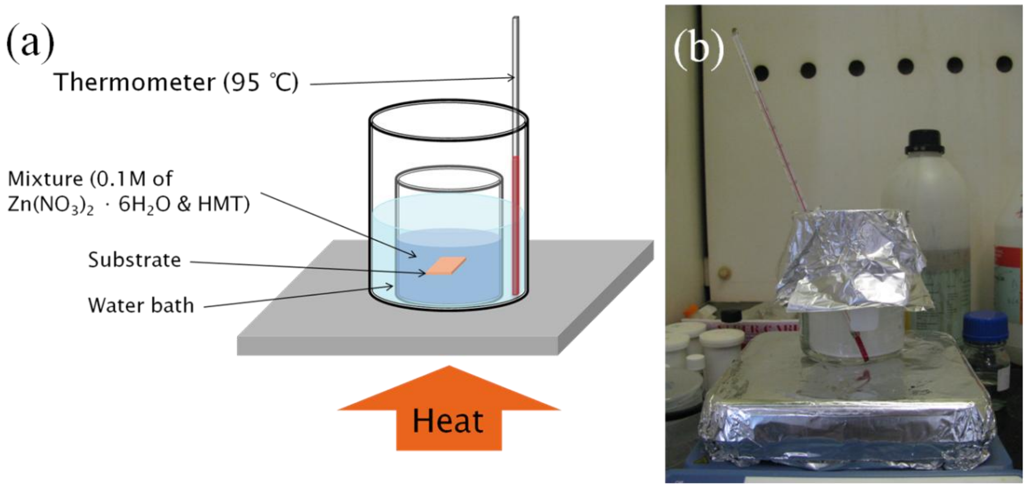

Figure 6.1 (a) Schematic diagram of the experimental setup for the growth of the ZnO nanorods and (b) Photograph of the setup.

6.3 Effects of buffer layer growth temperature

6.3.1 Structure characterization

Fig. 6.2 shows the XRD spectra of the ZnO nanorods grown on the buffer layers which are prepared at various temperatures. When the buffer layer is deposited at room temperature, a multiple peaks including (100), (002), (101) and (102) are observed from the spectra. As the substrate temperature increases, only (002) peak is dominated, which indicates that the ZnO nanorods grow along c-axis orientation. At high temperature, the improvement of the crystallinity of the ZnO buffer layer may lead to the enhanced crystal quality of the nanorods.

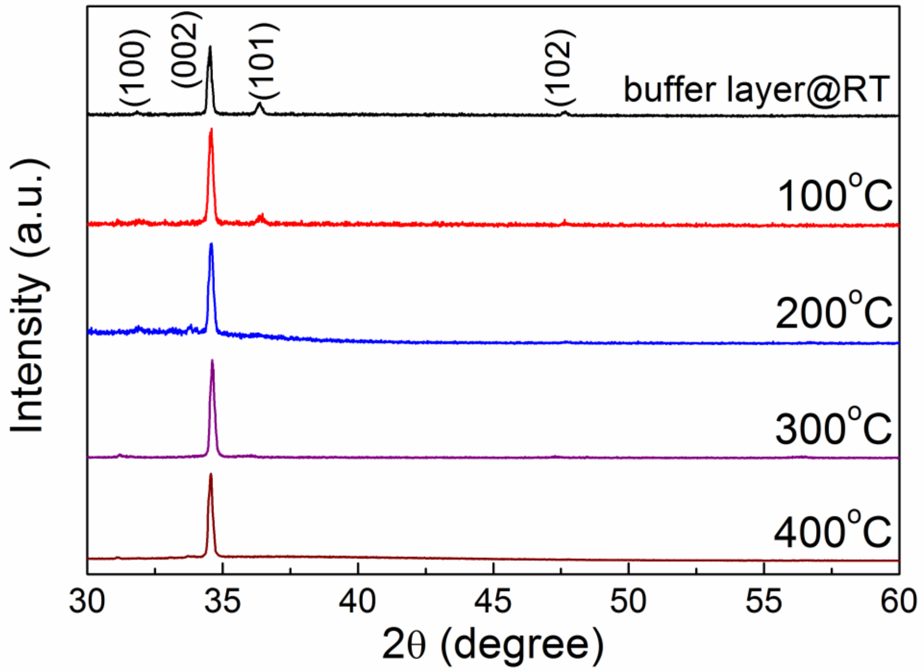

Figure 6.2 XRD spectra of the ZnO nanorods deposited on buffer layers prepared at various substrate temperatures.

Fig. 6.3 shows the SEM images of the ZnO nanorods on the ZnO buffer layer deposited at various substrate temperatures. It is shown that the orientation of the nanorods is affected by the growth temperatures of the buffer layers. At the low growth temperature, the nanorods align in different directions. The higher degree of alignment and converge density are observed when the buffer layer was deposited at higher temperature. At 400 ^{o}C, the nanorods become well-aligned perpendicular to the substrate. The observation is consistent with the XRD results. The quality of the buffer layer has a considerable effect on the alignment of the ZnO nanorods.

In addition, it is experimentally shown that the buffer layer is essential for the growth of ZnO nanorods by solution method. If the nanorods were grown without such a layer, they would be oriented randomly and adhered inadequately on the substrate. The difference between the region with and without buffer layer is shown in Fig. 6.4.

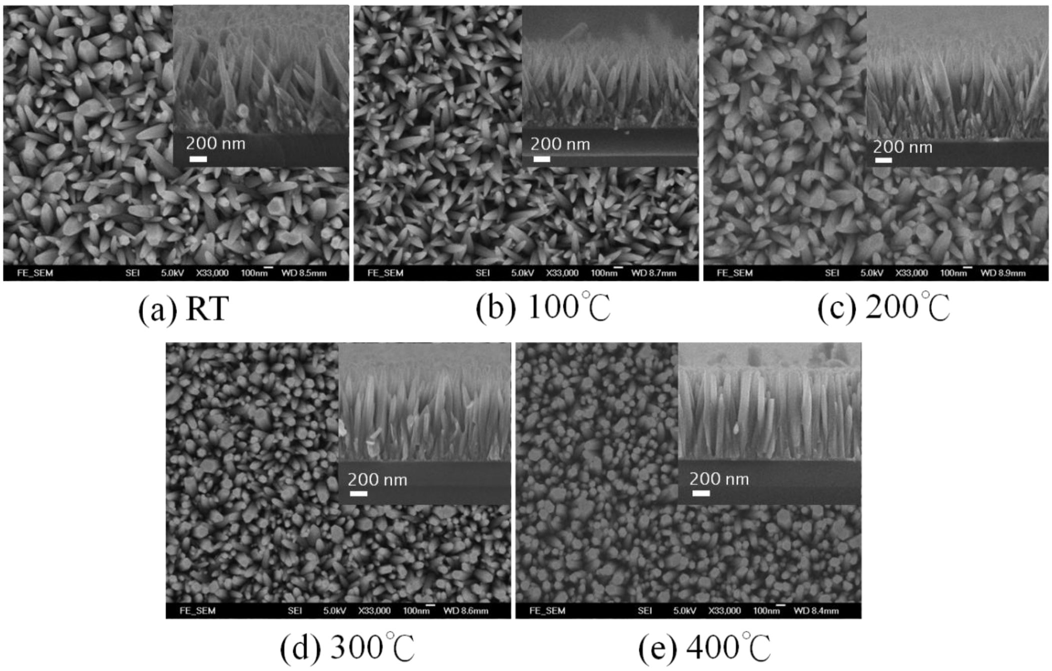

(a) RT (b) 100℃ (c) 200℃

(d) 300℃ (e) 400℃

Figure 6.3 SEM images of the ZnO nanorods grown on the buffer layer deposited at (a) room temperature, (b) 100 °C, (c) 200 °C, (d) 300 °C and (e) 400 °C. The insets show the cross-section view of the nanorods.

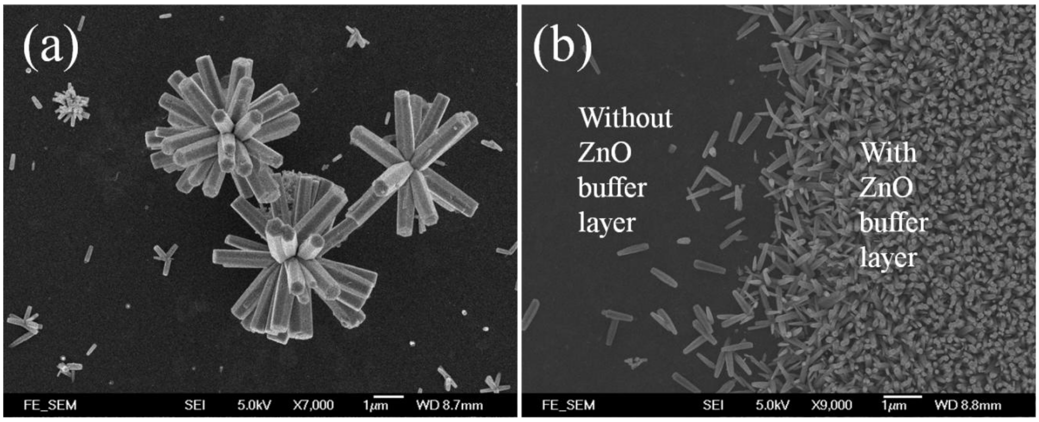

Figure 6.4 (a) SEM image shows the nanorods without buffer layer. (b) Difference between the region with and without buffer layer.

The TEM image of an individual ZnO nanorod is shown in Fig. 6.5 (a). The average diameter of the nanorods is about 70 nm with a sharp morphology. The lengths of the nanorods are ranged from 600 nm to 1μm. Fig. 6.5 (b) and (d) illustrate a preferential (002) orientation of a nanorod with its interplanar distance of ~ 0.26 nm. The result is confirmed by the select area electron diffraction pattern (Fig. 6.5 (c)), indicating the single crystalline structure of the nanorods.

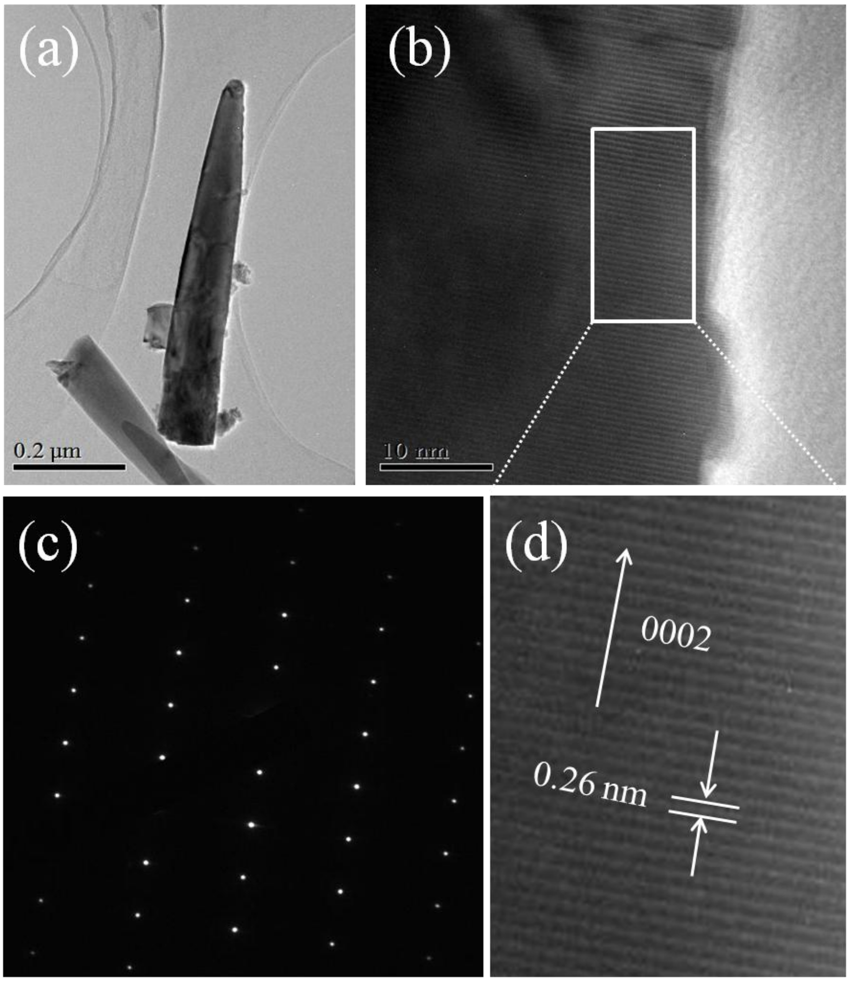

Figure 6.5 (a) TEM image of a single ZnO nanorod and its corresponding HRTEM image is shown in (b). (c) Selected area electron diffraction pattern of the ZnO nanorods. (d) The magnified region in (b) shows the [0002] orientation and the lattice spacing of the nanorods.

6.3.2 Photoluminescence

In order to investigate the optical properties of the ZnO nanorods, PL measurement was carried out at room temperature. Fig. 6.6 (a) depicts the PL spectra of the ZnO nanorods grown on the buffer layers deposited at various temperatures. All the samples exhibit a UV emission and a broad green emission band. The UV emission is peaked at around 380 nm which is originated from the exciton recombination corresponding to the near band edge emission. This free exciton recombination is generally come from the exciton-exciton collision [101, 102]. The green emission band is due to the point defects and such as oxygen vacancies, zinc interstitial or other impurities, which may be resulted from the recombination of a photogenerated hole with an electron associated with singly ionized oxygen vacancy [103, 104].

The PL intensity ratio of UV emission to the green emission band ($I_{UV}/I_{Visible}$) is shown in Fig. 6.6 (b). The average ratio is determined to be about 0.26. The results indicate that the PL of the ZnO nanorods only slightly depends on the buffer layer quality.

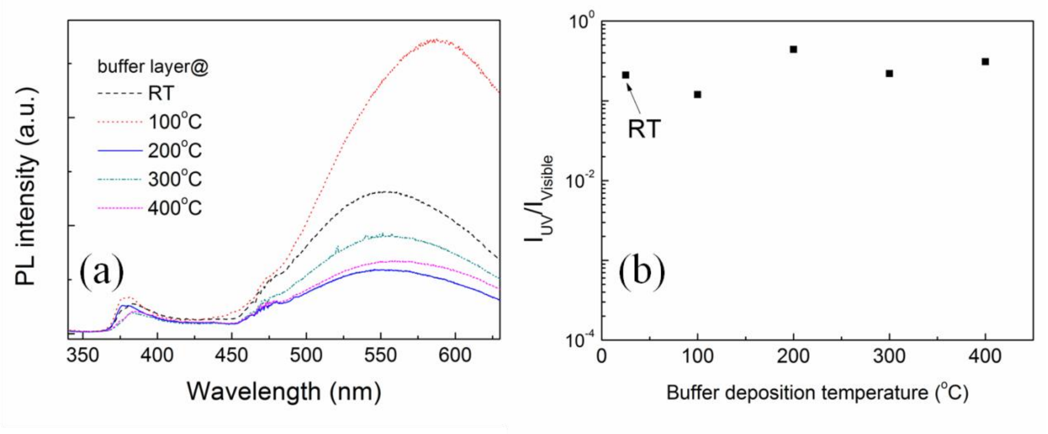

Figure 6.6 (a) PL spectra of the ZnO nanorods on the buffer layer deposited at various temperature and (b) PL intensity ratio of UV emission to visible band as a function of the buffer deposition temperature.

6.4 Effects of buffer layer thickness

6.4.1 Structural characterization

Fig. 6.7 shows the XRD spectra of the ZnO nanorods with various thicknesses of the buffer layer. The buffer layer prepared at the substrate temperature of 400 ^{o}C was used to investigate the thickness dependence. The (002) peak intensity increases with the buffer layer thickness, which shows that the degree of preferential c-axis orientation enhances with increasing the thickness of the buffer layer. The thicker buffer layer is made of stacking many preferred c-axis grains perpendicular to the substrate and favors the growth of the nanorods along c-axis [105].

On the other hand, the $2\theta_{(002)}$ value decreases from 34.6° to 34.52° when the buffer thickness increases from 20 to 100 nm. This may be attributed to the distribution of microstrain generated between the buffer layer and nanorods for thicker buffer layer.

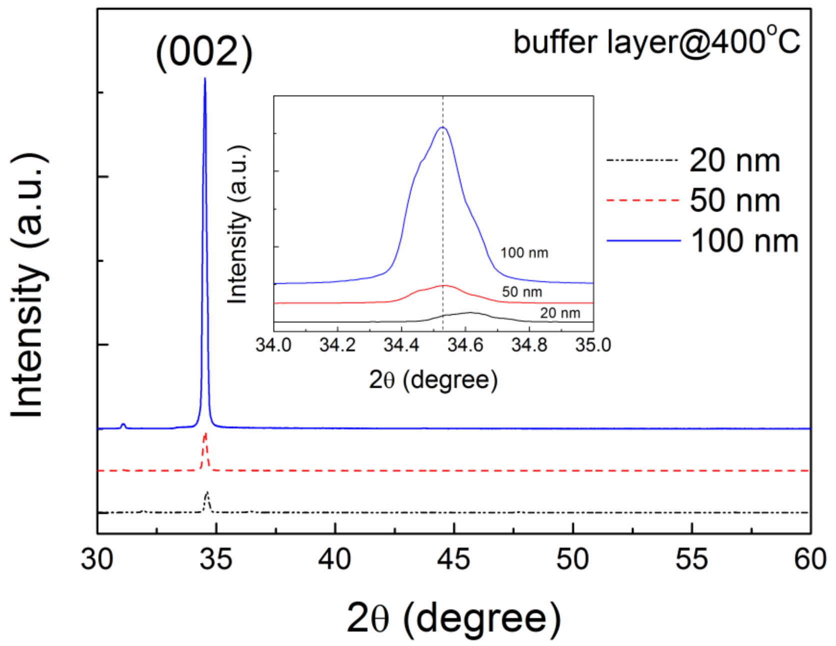

Figure 6.7 XRD spectra of the ZnO nanorods with different thicknesses of buffer layer. The inset shows the peak shift with the buffer layer thickness.

Fig. 6.8 illustrates the SEM images of the ZnO nanorods grown on different buffer thicknesses. Hexagonal shapes are observed in the plan-view SEM images. The nanorods grown on the thicker buffer layer have higher degree alignment of the columnar structures, making the nanorods growing close to each other and merge with the neighbor rods by the oriented attachment mechanism [106]. However, it can be found from the SEM images that the buffer layer thickness does not have major effect on the length and diameter of the nanorods.

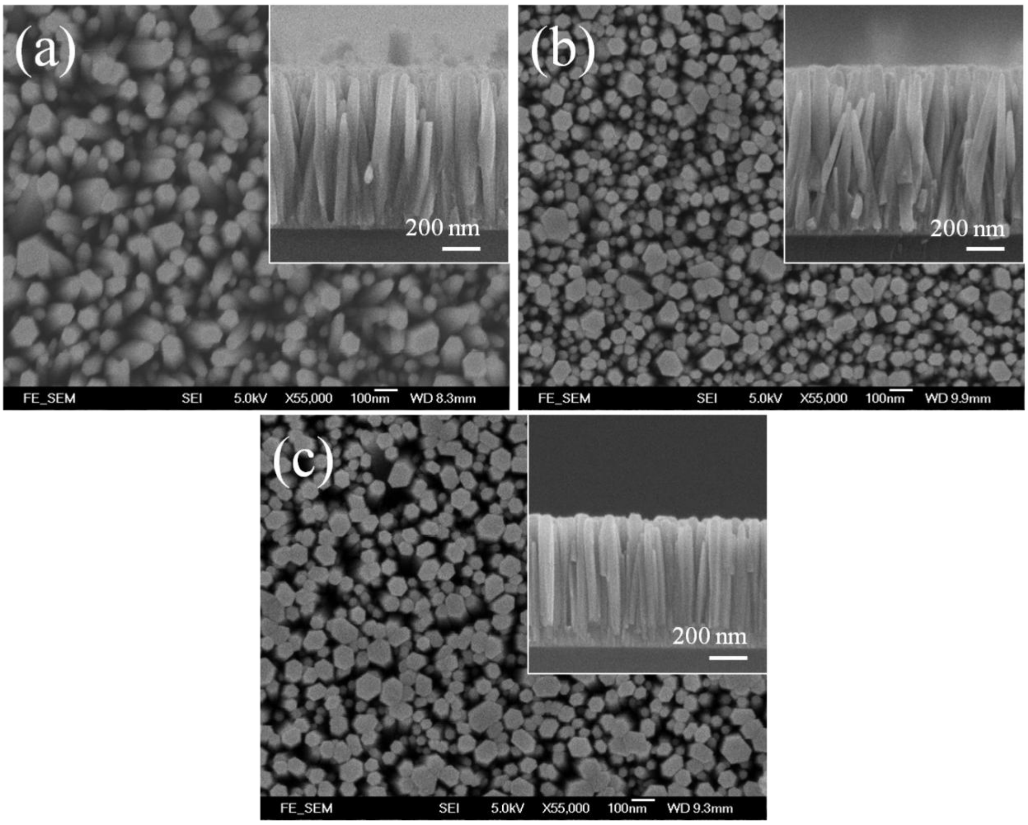

Figure 6.8 SEM images of the ZnO nanorods grown on the buffer layer with the thickness of (a) 20 nm, (b) 50 nm and (c) 100 nm. The inset shows the cross-sectional view of the nanorods.

6.4.2 Photoluminescence

The PL emission of the ZnO nanorods with different buffer layer thicknesses was also investigated. As shown in Fig. 6.9 (b), the $I_{UV}/I_{Visible}$ increases when the buffer layer thickness increases from 20 to 50 nm. This finding is attributed to the fact that the quality of the nanorods is enhanced with the thicker buffer layer. However, the $I_{UV}/I_{Visible}$ reduces with further increasing the thickness. Comparing with the XRD results, the strongest XRD peak occurs at the nanorods grown on the 100 nm-thick buffer layer, whereas the degraded PL is observed at that buffer thickness. The possible reason of the discrepancy between the XRD and PL might be due to the microstrain-induced change of structure in the ZnO nanorods. The structural change in the nanorods might result in crystalline defects.

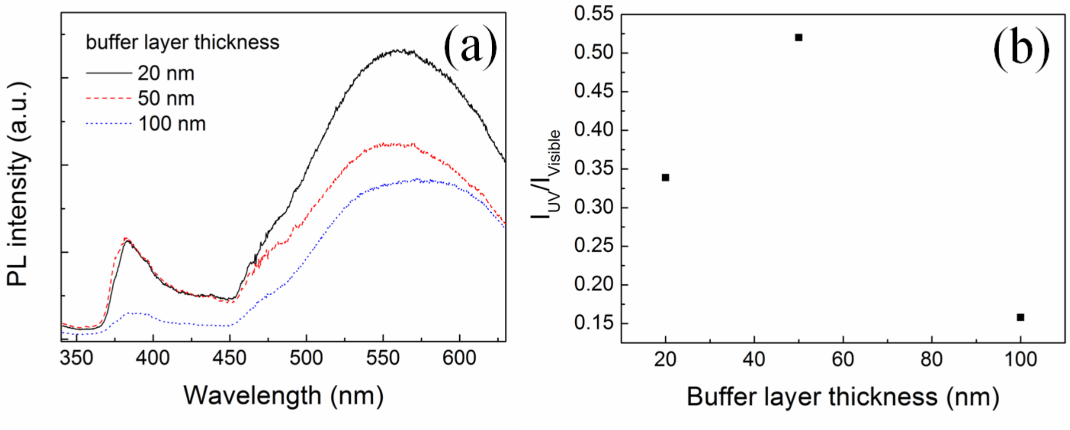

Figure 6.9 (a) PL spectra of the ZnO nanorods on the buffer layer with the thickness of (a) 20 nm, (b) 50 nm and (c) 100 nm. (b) PL intensity ratio of UV emission to visible band as a function of the buffer layer thickness.

6.5 Summary

In summary, the ZnO nanorods were synthesized by the chemical aqueous method at 95 ^{o}C. The effects of buffer layer grown temperature and thickness were studied. All the samples exhibited strong (002) orientation. At higher deposition temperature, the high degree of alignment and converge density of the nanorods were obtained. With the increase of the buffer layer thickness, the degree of preferential c-axis growth of the nanorods was enhanced due to the contribution of the grains in the buffer layer. PL measurement showed that all the nanorods demonstrated a UV emission at ~ 380 nm and a broad defect related green emission band. The PL intensity $I_{UV}/I_{Visible}$ ratios were determined as a function of the buffer layer grown temperature and thickness. The growth temperature of the buffer layer has minor effect on the PL emission of the nanorods. On the other hand, the reduction of the $I_{UV}/I_{Visible}$ ratio was observed for the nanorods with the thicker buffer layer.

Chapter 7 Fabrication and characterization of hybrid light-emitting diodes

7.1 Introduction

Zinc oxide (ZnO) is a promising semiconductor for light-emitting diodes (LEDs) [107-110] and laser diodes (LDs) [111]. The reason for the use of ZnO is not only due to its optical properties, but also the existence of deep-defect levels which can emit various colors covered from ultraviolet (UV) to visible spectrum. Electrically and optically pumped ZnO-based devices have been demonstrated [107-110]. Among these results, the ZnO films grown on various substrates such as *p*-GaN [107], *p*-NiO [108], *p*-SiC [109] and *p*-Si [110] have been widely investigated. Long *et al*. [108] have fabricated ZnO/NiO heterojunction LEDs which exhibited UV emission peaked at ~ 370 nm. In recent years, ZnO-organic hybrid LEDs have attracted world-wide attention. It has been shown that inorganic and organic semiconductors are able to form a device to realize emission from both kinds of materials [112]. Bolink *et al.* [113] fabricated ZnO/organic LEDs with the use of poly(9,9-dioctylfluorene-*co*-benzothiadiazole) (F8BT). Zhao *et al*. [114] prepared ZnO/MEH-PPV heterostructure LEDs and the devices exhibited a sharp UV emission and a broad visible emission. Subsequently, electroluminescence (EL) from ZnO/PFO hybrid LEDs have been reported by Bano *et al* [115]. They found a white light emission from 450 nm to 620 nm under forward bias.

On the other hand, ZnO can be processed in large variety of nanostructures which can be grown on substrate without the need of lattice matching. ZnO nanorods may offer advantages for light emission due to the improved carrier confinement and increased junction area in 1-D nanostructures [116, 117]. The growth of ZnO nanorods can be performed by either high-temperature [118] or low-temperature (<100℃) [119, 120] growth techniques. It is preferred to use low-temperature approach to grow ZnO nanorods because it is possible for the fabrication of electronic and photonic devices on plastic substrates. Nadarajah *et al*. [121] reported EL from flexible ZnO/organic LEDs. In their work, ZnO nanowires were electrodeposited at 80℃ on flexible polymeric substrate. The combination of low-temperature grown ZnO nanorods and organic semiconductor likely provides an alternative approach for the fabrication of solid state lighting devices. In this chapter, we synthesized the ZnO nanorods onto Si substrate by low-temperature aqueous chemical method. The as-grown ZnO nanorods were then utilized to fabricate hybrid heterojunction LEDs with a *p*-type organic N, N’-diphenyl-N, N’-bis(1-naphthyl)-1, 1’-biphenyl-4, 4’-diamine (α-NPD). The α-NPD used here is one of the most widely used hole transport and blue-emitting organic semiconductors.

7.2 Fabrication

Fig. 7.1 shows the fabrication process of the hybrid LED. Prior to the ZnO nanorods growth, the Si substrate was cleaned by acetone and isopropyl alcohol in ultrasound bath for 15 minutes respectively, then it was etched by HF (10%) acid to remove the native oxide on the Si surface. After cleaning, a ~ 20 nm-thick ZnO buffer layer was deposited onto the *n*-type doped Si substrate by filtered cathode vacuum arc technique. During the deposition, the oxygen flow rate and substrate temperature were kept at 40 SCCM and 200 ℃, respectively. The ZnO nanorods were then directly grown on the buffer layer. The growth method is described in detail in Chapter 3. After the growth of the nanorods, polymethyl methacrylate (PMMA) was spin-coated onto the ZnO nanorods in order to insulate the uncovered ZnO buffer layer area. A α-NPD layer of ~ 150 nm was directly deposited on the top of the ZnO nanorods by thermal evaporation without substrate heating. Finally, a molybdenum trioxide (MoO_3) layer and an Al electrode (anode) with thicknesses of ~ 10 nm and ~ 100 nm, respectively were evaporated onto the samples. Ag paste was used as the bottom electrode (cathode) of Si. The use of a thin MoO_3 layer has been shown to enhance the hole injection between the electrode and organic layer [122] and to act as a protective layer of organic material [123]. Instead of Si, the similar structures were also fabricated on the ITO glass with the same condition, except that the ITO glass was cleaned by oxygen-plasma with a power of about 20 W under the partial pressure ranged from 400 to 500 mTorr to remove the surface contamination.

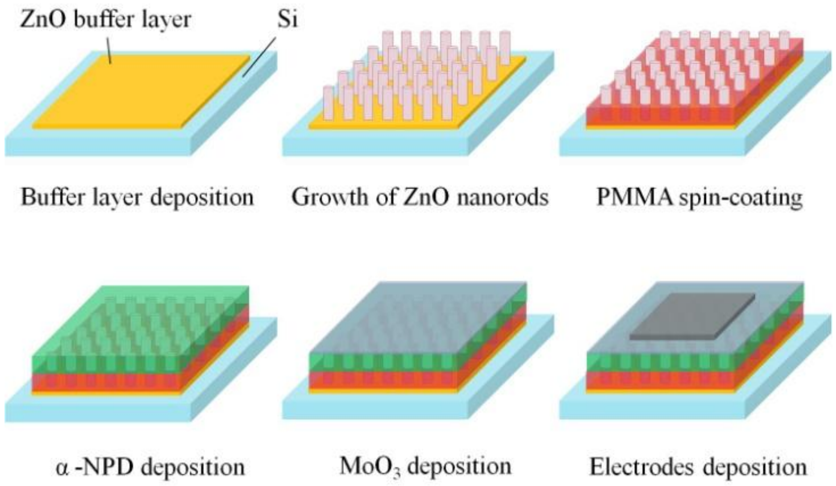

Figure 7.1 Fabrication process of the hybrid structure.

7.3 Structural properties of the ZnO nanorods

The SEM images of the ZnO nanorods are shown in Fig. 7.2. A large scale and uniform ZnO nanorods are grown on the Si, as shown in Fig. 7.2(a). The inset depicts that the ZnO nanorods have a hexagonal geometry with a smooth top surface. The diameter of the ZnO nanorods is in the range from 50 to 90 nm. The cross sectional SEM image (Fig. 7.2(b)) reveals clearly that the ZnO nanorods are grown on the ZnO buffer layer and are synthesized predominantly perpendicular to the Si substrate along c-axis orientation. The average length of the nanorods is about 1 μm. The aspect ratio, which defines as the length of a nanorod divided by the width, is calculated to be around 15.

The SEM image of the ZnO nanorods grown on the ITO glass is illustrated in Fig. 7.2 (c). The morphology and alignment of the as-grown nanorods on ITO glass appears different from those on Si substrate. The nanorods grown on the Si likely aligned better than those on ITO glass, probably depending on the roughness of the substrate.

The XRD pattern of the ZnO nanorods is shown in Fig. 7.2 (d). All the diffraction peaks can be indexed to the hexagonal wurtzite structure of ZnO. The intensity of (002) peak is the strongest among those peaks, verifying high crystal quality and preferable c-axis orientation.

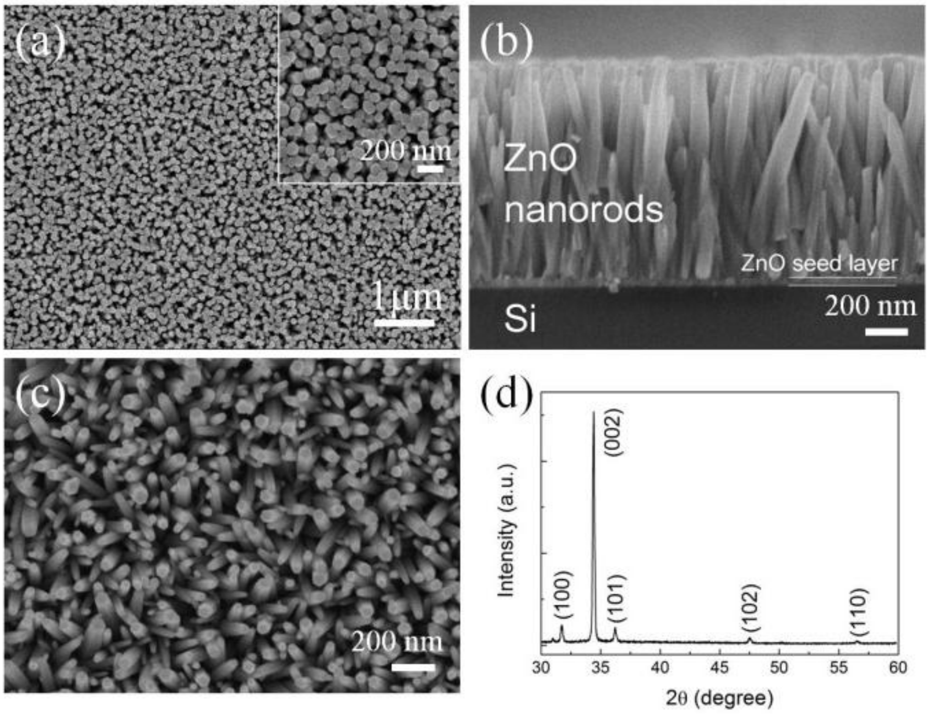

Figure 7.2 (a) The top view and (b) cross section SEM images of the as-grown ZnO nanorods. (c) The ZnO nanorods grown the ITO glass. (d) XRD pattern of the ZnO nanorods grown on the Si.

7.4 Electrical properties of the hybrid structures

The room-temperature I-V characteristics of the diodes are shown in Fig. 7.3 (a). It is observed that both diodes exhibit rectifying diode-like behavior. The turn-on voltage of the α-NPD/ZnO/Si diode is ~ 3.4 V, which is ~ 0.9 V lower than that of the α-NPD/ZnO/ITO diode. The inset of Fig. 7.3 (a) depicts the I-V characteristic of the Al/MoO_3 contacts deposited onto the α-NPD. The configuration of the measurement of Al/MoO_3/α-NPD is demonstrated in Fig. 7.3 (b). The distance between the two electrodes is 1.5 mm. The I-V curve of the Al/MoO_3/α-NPD shows a fairly ohmic behavior. Hence, it can be proved that the rectifying diode-like behavior is mainly due to the formation of *p-n* junction between the ZnO nanorods and the α-NPD layer. On the other hand, the measured leakage current of the ZnO/α-NPD/Si structure at reverse bias voltage of -14 V is less than ~ 70 μA, which is lower than that of ZnO/α-NPD/ITO structure (~ 0.15 mA). This is because a thin SiO_x might be formed between the ZnO buffer layer and Si substrate during the growth of ZnO buffer layer. The SiO_x layer at the ZnO/n-Si interface acts as a Schottky barrier and hence the electron might tunnel from the n-Si valence band to ZnO conduction band at reverse bias.

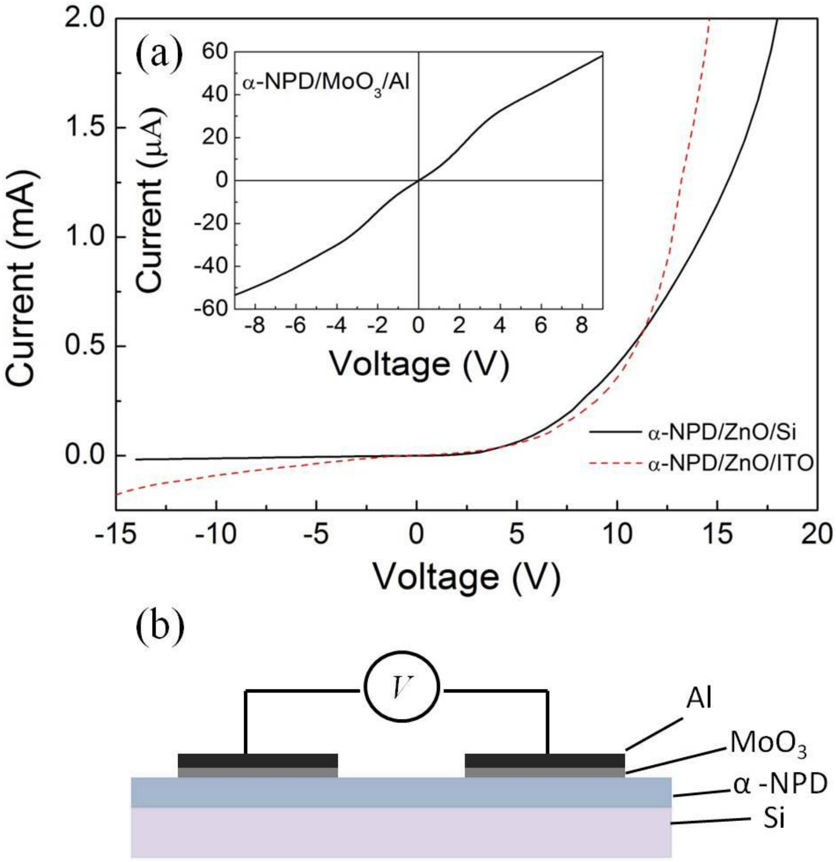

Figure 7.3 (a) Room temperature I-V characteristics of the α-NPD/ZnO/Si and α-NPD/ZnO/ITO heterojunction LEDs. (b) The configuration of the α-NPD contacts ohmic measurement.

7.5 Optical properties

7.5.1 Photoluminescence

Fig. 7.4 depicts the room temperature PL spectra of the ZnO nanorods and *α*-NPD layer. The PL spectrum of the *α*-NPD exhibits a strong blue peak at ~ 440 nm. For the nanorods, the spectrum shows a sharp ultraviolet (UV) emission at ~ 380 nm and a broad visible emission at ~ 560 nm. The UV emission is generally ascribed to near-band-edge emission commonly related to free exciton recombination through exciton-exciton collision. As for the origin of the yellowish green emission, it is typically attributed to deep-level emission associated with the recombination of photon generated holes with intrinsic defect complexes, which likely include zinc or oxygen vacancy complexes [124].

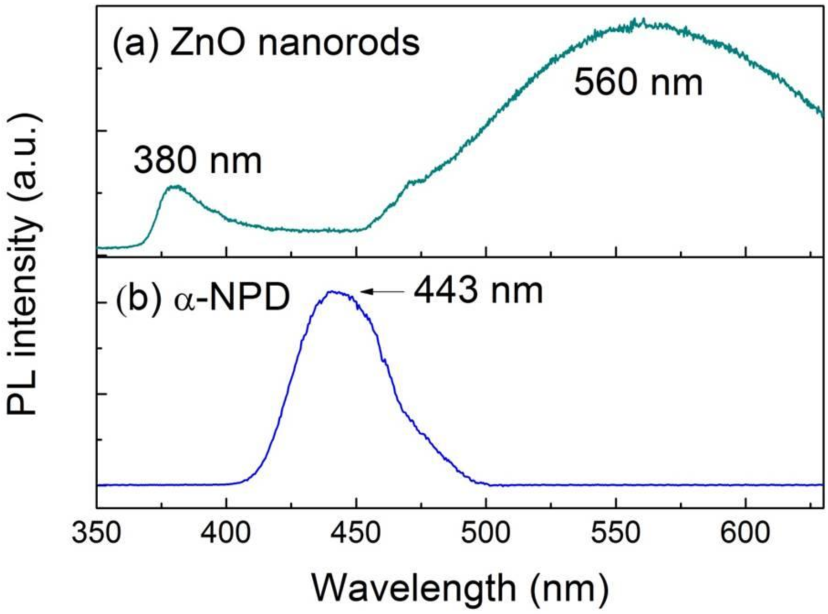

Figure 7.4 PL spectra of the (a) ZnO nanorods and (b) α-NPD layer.

7.6 Electroluminescence

The EL spectra from the hybrid LEDs at different forward-biased voltages are shown in Fig. 7.5. It is observed that at the biased voltage of ~ 15 V, a broad blue emission emerges from the EL spectrum with a band at ~ 464 nm. The emission intensity increases as the biased voltage increases. The EL spectrum obtained for the diode is fitted by three Gaussian curves which are dominated by 467 nm, 520 nm and 633 nm, as shown in Fig. 7.5 (c). The EL peaks are comparable to the PL spectra of the ZnO nanorods and α-NPD layer. The blue emission at 467 nm is emerged from the α-NPD layer. This agrees well with the previous report [125]. On the other hand, the emission at 520 nm (green) and 633 nm (orange-red) can be associated with the intrinsic deep level defects in ZnO. The origin of green band is the most investigated and the most controversial band in ZnO. The variation of green emission may be resulted from different intrinsic defects such as zinc vacancy (V_{Zn}), oxygen vacancy (V_O), interstitial zinc (Zn_i), interstitial oxygen (O_i) and antisite oxygen (O_{Zn}). Sun *et al.* [126] theoretically predicted the intrinsic defect levels in ZnO. The calculated defect energy level is illustrated in Fig. 7.5 (e). It is shown that the energy interval from the bottom of conduction band to O_{Zn} is consistent with the energy of green emission (2.38 eV) in our experiment. On the other hand, the energy interval (2.28 eV) between the bottom of conduction band and O_i approximately confirms the green band. However, the probability of forming O_i is relatively low due to the larger diameter of oxygen atom as compared to zinc atom. Hence, we suggest that the green emission is associated with the electron transition from the bottom of conduction band to O_{Zn} level. The orange-red emission is ascribed to the transition from Zn_i level to O_{Zn} level.

Because the green luminescence has also been shown to appear at the interface of ZnO/Si heterojunction LEDs [127], hybrid LEDs on the ITO glass were prepared to identify the emission. The corresponding EL spectrum is shown in Fig. 7.5 (b). The turn-on voltage for the α-NPD/ZnO/ITO heterojunction LED is lower than that of the LED grown on Si. It might be due to the high carrier injection in the ITO as compared to that of Si. The Gaussian fitting of EL spectrum obtained from the diode is shown in Fig. 7.5 (d). The EL spectrum is dominated at 477 nm, 552 nm and 640 nm, which is similar to the spectrum of the α-NPD/ZnO/Si diode. Hence, it is confirmed that the green luminescence is attributed to the deep-defect level of ZnO nanorods and the EL spectrum is substrate-independent.

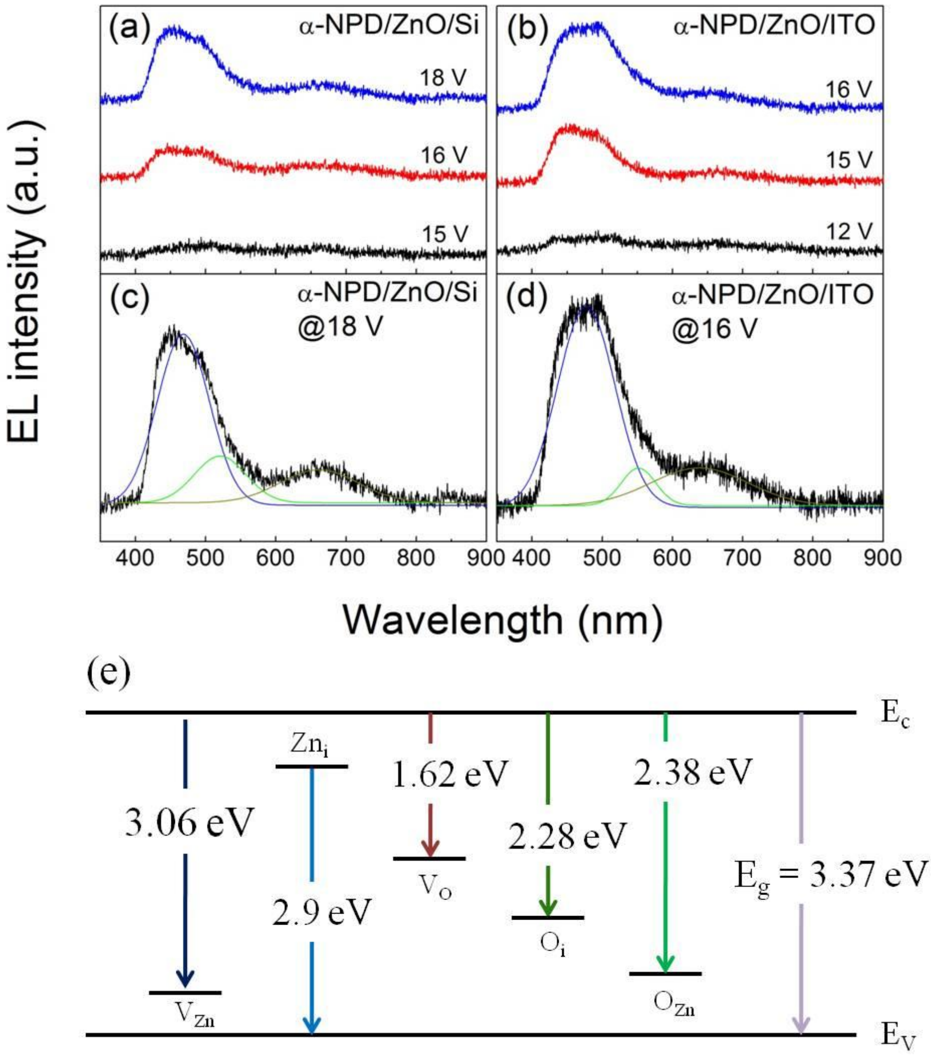

Figure 7.5 EL spectra of the (a) *α*-NPD/ZnO/Si and (b) *α*-NPD/ZnO/ITO structures. (c) and (d) Gaussian fitting of the EL spectrum of the corresponding diodes. (e) Calculated deep-defect level energy diagram of ZnO.

In order to understand the mechanism of the light emission, the EL of the hybrid LED is examined by using energy-band diagram, as shown in Fig. 7.6. The band gap energy of ZnO (3.36 eV) is nearly equivalent to that of *α*-NPD (3.1 eV). The energy affinities of Si, ITO, ZnO and lowest-unoccupied molecular orbital (LUMO) of α-NPD can be assumed to be 4.05 eV [128], 4.5 eV [129], 4.35 eV

[130] and 2.5 eV [131], respectively. For ZnO/α-NPD interface, it is shown that the energy band offsets between conduction band-lowest-LUMO (~ 1.9 eV) and valence band-highest occupied molecular orbital (HOMO) (~ 2 eV) are comparable, suitable for charge transfer from organic to inorganic semiconductor, or from inorganic to organic semiconductor. Under large forward-bias voltage, holes can be injected from the HOMO of the α-NPD to the valence band of the ZnO. Electrons excited to the conduction band of the ZnO can be relaxed nonradiatively to the trap-level states and radiatively recombined with holes near the valence band of the ZnO. At the same time, electrons from the conduction band of the ZnO can be injected to LUMO of the α-NPD, and radiatively recombined with holes in the HOMO of the α-NPD. According to the PL and EL spectra of the ZnO nanorods and α-NPD, it is suggested that both electron and hole transfer are dominated for radiative emission. On the other hand, for the ZnO/α-NPD/Si heterojunction, the valence band offset (> 2 eV) between ZnO and Si is relatively large. With the replacement of Si with ITO, the valence band offset between the ZnO and the ITO becomes as small as ~ 0.3 eV. Hence, holes are able to tunnel through the barrier of the valence band of the ZnO for the ZnO/α-NPD/ITO heterojunction, leading to larger leakage current under reverse bias.

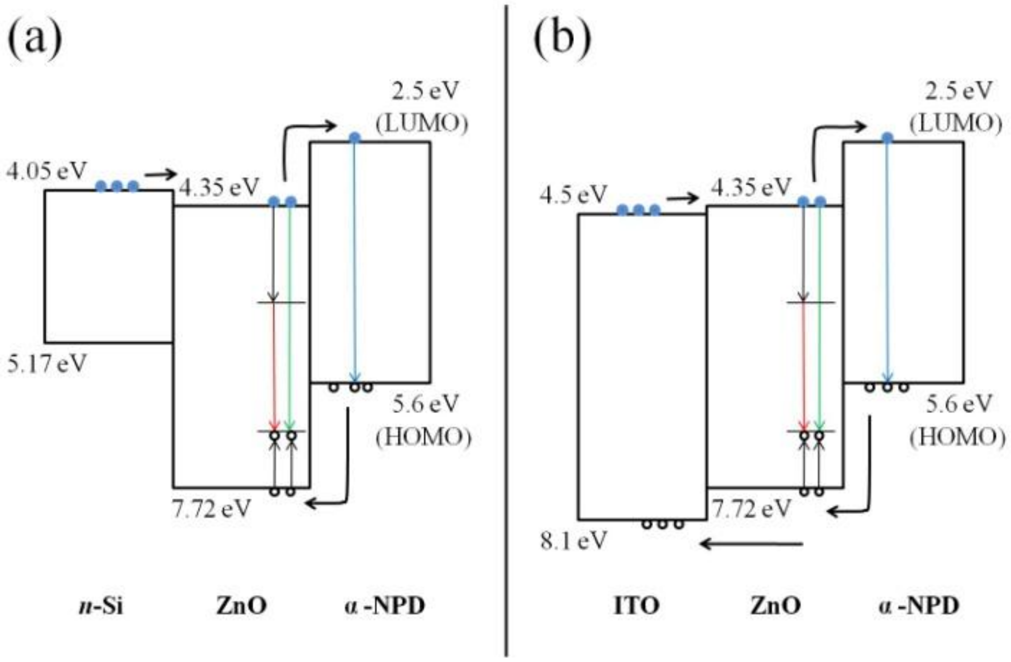

Figure 7.6 Energy band diagram of the α-NPD/ZnO/Si (a) and α-NPD/ZnO/ITO (b) heterojunction under forward bias.

On the other hand, the EL from the organic component can be explained by Föster energy transfer from inorganic to organic component [132]. Such concept has been used to achieve light amplification in optically pumped organic layer [133]. The basic idea of this approach is to utilize the electrical pumping of inorganic material to produce the luminescence of organic material when the EL spectrum of the inorganic layer overlaps the absorption spectrum of the organic layer. Consequently, it results in a strong coupling of inorganic layer excitation to the adsorption dipole of organic layer. In this case, the α-NPD has a broad absorption band in UV regime [125]. However, the emission from the α-NPD layer is not likely due to the absorption from the ZnO nanorods because the dominant EL band of the ZnO is weaker than the absorption band of the α-NPD. Hence, the EL from the organic layer is attributed to the radiative recombination of the electron-hole pairs in both organic and inorganic layers.

7.7 Summary

Hybrid *p-n* heterojunction LEDs were fabricated using ZnO nanorods and organic semiconductors. The diodes exhibited a rectifying diode-like behaviour. The EL of the devices revealed a blue emission originated from the organic material as well as yellowish-green emission due to the deep-defect levels from the ZnO nanorods. It is believed that the emission is originated from the radiative recombination of the injected carriers in both organic and inorganic components.

Chapter 8 Conclusion and recommended future works

8.1 Conclusion

In this project, the ZnO and ZnO:Al thin films were deposited on SiO_2/Si by FCVA technique at various substrate temperatures. The in-depth studies were carried out to investigate the structural, electrical as well as optical properties of the ZnO and ZnO:Al films. The crystal quality of the films was enhanced with an increase in substrate temperature. The electrical resistivity of the films decreased gradually when the substrate temperature increased. PL measurement was carried out to study the optical quality. All the samples exhibited a UV emission band at room temperature, which is associated with free excitonic recombination. The broadening of the PL spectra was observed with increasing doping concentration due to the Burstein-Moss shift. Transmittance spectra showed that all the films exhibited a high transparency (~ 85 %) in the visible regions. The energy band gap was determined in accordance of the transmittance spectra.

The ZnO and ZnO:Al (7%) films were utilized to fabricate a heterojunction LED by vertical contact approach. The LEDs exhibited room temperature EL luminescence peaked at ~ 370 nm. The EL was attributed to the radiative recombination within the ZnO:Al (7%) and ZnO films.

ZnO nanorods have been grown by a low temperature aqueous method. The effects of the buffer layer deposition temperature and the thickness were studied via the structural and optical measurements. The degree of the ZnO nanorods alignment was improved with the increase of deposition temperature of the buffer layer and the thickness. PL measurement showed that the emission was independent on the buffer deposition temperature; however, The PL emission was found to be decreased with the thicker buffer layer.

The as-grown ZnO nanorods were used as an electron injector to fabricate hybrid LEDs with a p-type organic semiconductor, N, N'-diphenyl-N, N'-bis(1-naphthyl)-1, 1'-biphenyl-4, 4'-diamine (α-NPD). The LEDs were fabricated on the n-Si and ITO glass respectively. Both of the LEDs showed a blue emission band originated from α-NPD layer, showing that the EL is substrate independent. The origin of the EL was explained in terms of the energy band diagram.

8.2 Recommended future works

The study presented in this thesis is focused on the fabrication of the ZnO-based LEDs. Although comprehensive studies have been performed to investigate the luminescence, reproducible and high quality p-type ZnO remains challenges. Therefore, it is highly desirable to prepare p-type ZnO with large carrier concentration to fabricate more efficient homojunction LEDs.

In this thesis, LEDs based on the ZnO nanorods were also demonstrated. However, defect-related emission is observed from the ZnO nanorods. In order to improve the optical properties, the optimized condition for the growth of the nanorods is needed to be determined. In addition, optoelectronic applications on flexible polymeric substrate are possible for the low temperature growth of the ZnO nanorods.

References

[1] The status of silicon carbide and related materials, III-Vs review 9, 58 (1996).

[2] V. Benda, J. Gower and D. A. Grant, 'Power Semiconductor Devices: Theory and Applications', John Wiley & Sons (1999).

[3] D. C. Reynolds, D. C. Look and B. Jogai, 'Optically pumped ultraviolet lasing from ZnO', Solid State Commun. 99, 873 (1996).

[4] M. Kawasaki, A. Ohtomo, I. Ohkubo, H. Koinuma, Z. K. Tang ,P. Yu, G. K. L. Wong, B. P. Zhang and Y. Segawa, 'Excitonic ultraviolet laser emission at room temperature from naturally made cavity in ZnO nanocrytal thin films', Mater. Sci. Eng. B-Solid State Mater. Adv. Technol. 56, 239 (1998).

[5] D. M. Bagnall, Y. F. Chan, Z. Zhu, T. Yao, S. Koyama, M. Y. Shen and T. Goto, 'Optically pumped lasing of ZnO at room temperature', Appl. Phys. Lett. 70, 2230 (1997).

[6] D. C. Look, D. C. Reynolds, J. W. Hemsky, R. L. Jones anf J. R. Sizelove, 'Production and annealing of electron irradiation damage in ZnO', Appl. Phys. Lett. 75, 811 (1999).

[7] Z. Z. Ye, J. G. Liu, Y. Z. Zhang, H. P. He, ZnO: Doping and Application, Zhejiang University Press, pp. 5-6 (2009).

[8] D. C. Look, J. W. Hemsky, and J. R. Sizelove, 'Residual native shallow donor in ZnO', *Phys. Rev. Lett.*, vol. 82, no. 12, pp. 2552–2555 (1999).

[9] C. G. Van deWalle, "Hydrogen as a cause of doping in zinc oxide",

Phys. Rev. Lett., vol. 85, no. 5, pp. 1012–1015 (2000).

[10] M. S. Oh, D. K. Hwang, J. H. Lim, Y. S. Choi, and S. J. Park, ‘Currentdriven hydrogen incorporation in zinc oxide’, Phys. Rev. Lett., vol. 91, no. 21, p. 212 102, Nov. 2000.

[11] André Anders, Sunnie H.N. Lim, Kin Man Yu, Joakim Andersson, Johanna Rosén, Mike McFarland, and Jeff Brown, ‘High quality ZnO:Al transparent conducting oxide films synthesized by pulsed filtered cathodic arc deposition’, eScholarship, University of California (2009).

[12] Q. B. Ma, Z. Z. Ye, H. P. He, J. R. Wang, L. P. Zhu, B. H. Zhao, ‘Substrate temperature dependence of the properties of Ga-doped ZnO films deposited by DC reactive magnetron sputtering’, Vacuum 82, 9 (2008).

[13] N. Ito, Y. Sato, P.K. Song, A. Kaijio, K. Inoue and Y. Shigesato, ‘Electrical and optical properties of amorphous indium zinc oxide films’, Thin Solid Films 496, 99 (2006).

[14] O. F. Schirmer and D. Zwingel, “The yellow luminescence of zinc oxide,” Solid State Commun., vol. 8, no. 19, pp. 1559–1563, (1970).

[15] O. F. Schirmer, ‘The structure of the paramagnetic lithium center in zinc oxide and beryllium oxide’, J. Phys. Chem. Solids, vol. 29, no. 8, pp. 1407–1429, (1968).

[16] A. Valentini, F. Quaranta, M. Rossi, and G. Battaglin, ‘Preparation and characterization of Li-doped ZnO films’,J. Vac. Sci. Technol. A, Vac. Surf. Films, vol. 9, no. 2, pp. 286–289, (1991).

[17] L. L. Yang, Z. Z. Ye, L. P. Zhu, Y. J. Zeng, Y. F. Lu, and B. H. Zhao,

‘Fabrication of p-type ZnO thin films via DC reactive magnetron sputtering by using Na as the dopant source’, *J. Electron. Mater.*, vol. 36, no. 4, pp. 498–501, (2007).

[18] Y. Kanai, ‘Admittance spectroscopy of ZnO crystals containing Ag’, *Jpn. J. Appl. Phys.*, vol. 30, no. 9R, pp. 2021–2022, (1991).

[19] J. G. Lu, Y. Z. Zhang, Z. Z. Ye, L. P. Zhu, L. Wang, B. H. Zhao, and Q. L. Liang, “Low-resistivity, stable p-type ZnO thin films realized using a Li–N dual-acceptor doping method,” Appl. Phys. Lett., vol. 88, no. 22, pp. 222 114, (2006).

[20] T. H. Vlasenflin and M. Tanaka, ‘p-type conduction in ZnO dualacceptor- doped with nitrogen and phosphorus’, Solid State Commun., vol. 142, no. 5, pp. 292–294, (2007).

[21] Y. R. Ryu, S. Zhu, D. C. Look, J. M. Wrobel, H. M. Jeong, and H. W. White, “Synthesis of p-type ZnO films,” J. Cryst. Growth, vol. 216, no. 1, pp. 330–334, (2000).

[22] Y. R. Ryu, T. S. Lee, and H. W. White, “Properties of arsenic-doped p-type ZnO grown by hybrid beam deposition,” Appl. Phys. Lett., vol. 83, no. 1, pp. 87–89, Jul. 2003.

[23] T. Aoki, Y. Shimizu, A. Miyake, A. Nakamura, Y. Nakanishi, and Y. Hatanaka, ‘p-type ZnO layer formation by excimer laser doping’, Phys. Stat. Sol. (B), vol. 229, no. 2, pp. 911–914, Jan. 2002.

[24] J. H. Lim, C. K. Kang, K. K. Kim, I. K. Park, D. K. Hwang, and S. J. Park, “UV electroluminescence emission from ZnO light-emitting diodes grown by high-temperature radiofrequency sputtering,” Adv. Mater., vol. 18, no. 20, pp. 2720–2724, (2006).

[25] Y. R. Ryu, T. S. Lee, J. A. Lubguban, H. W. White, B. J. Kim, Y. S. Park, and C. J. Youn, ‘Next generation of oxide photonic devices: ZnO-based ultraviolet light emitting diodes’, Appl. Phys. Lett., vol. 88, no. 24, p. 241 108, Jul. 2006.

[26] Z. P. Wei, Y. M. Lu, D. Z. Shen, Z. Z. Zhang, B. Yao, B. H. Li, J. Y. Zhang, D. X. Zhao, X. W. Fan, and Z. K. Tang, ‘Room temperature p-n ZnO blue-violet light-emitting diodes’, Appl. Phys. Lett., vol. 90, no. 4, p. 042 113, (2007).

[27] J. Y. Kong, S. Chu, M. Olmedo, L. Li, Z. Yang, and J. L. Liu, ‘Dominant ultraviolet light emissions in packed ZnO columnar homojunction diodes’, Appl. Phys. Lett., vol. 93, no. 13, p. 132 113, (2008).

[28] D. H. Sankur and J. T. Cheung, ‘Highly oriented ZnO films grown by laser evaporation’, J. Vac. Sci. Technol. A, v1, n4, p 1806-1809 (1983).

[29] D.C. Look, D. C. Reynolds, J. R. Sizelove, R. L. Jones, C. W. Litton, G. Cantwell and W. C. Harsch, ‘Electrical properties of bulk ZnO’, Solid State Commun. 105, 399 (1998).

[30] J. E. Nause, ‘ZnO broadens the spectrum’, III-Vs Review 12, 28, 1999.

[31] M. Suscavage, M. Harris, D. Bliss, P. Yip, S. Q. Wang, D. Schwall, ‘High quality hydrothermal ZnO crystals’, MRS. Internet J. Nitride Semicond. Res. 4, U294 (1999).

[32] J. Ma, F. Ji, H. L. Ma and S. Y. Li, ‘Electrical and optical properties of ZnO: Al films prepared by an evaporation method’, Thin Solid Films 279, 213 (1996).

[33] C. C. Lin, S. Y. Chen, S. Y. Cheng, and H. Y. Lee, ‘Properties of

nitrogen-implanted p-type ZnO films grown on Si3N4/Si by radiofrequency magnetron sputtering', Appl. Phys. Lett. 84, no. 24, pp. 5040 (2004).

[34] B. Xiang, P. Wang, X. Zhang, S. A. Dayeh, D. P. R. Aplin, C. Soci, D. Yu, and D. Wang, 'Rational synthesis of p-type zinc oxide nanowires arrays using simple chemical vapor deposition', Nano Lett., vol. 7, no. 2, pp. 323–328 (2007).

[35] S. K. Hong, T. Hanada, H. J. Ko, Y. Chen, T. Yao, D. Imai, K. Araki and M. Shinohara, 'Control of polarity of ZnO films grown by plasma-assisted molecular-beam epitaxy: Zn- and O-polar ZnO films on Ga-polar GaN templates', Appl. Phys. Lett. 77, 3571 (2000).

[36] X. Pan, Z. Ye, J. Li, X. Gu, Y. Zeng, H. He, L. Zhu, and Y. Che, 'Fabrication of Sb-doped p-type ZnO thin films by pulsed laser deposition', Appl. Surf. Sci., vol. 253, no. 11, pp. 5067–5069 (2007).

[37] L. Armelao, M. Fabrizio, S. Gialanella and F. Zordan, 'Sol–gel synthesis and characterisation of ZnO-based nanosystems', Thin Solid Films 394, 90 (2001).

[38] D. H. Zhang and D. E. Brodie, 'Transparent conducting ZnO films deposited by ion-beam-assisted reactive deposition', Thin Solid Films 213, 109 (1992).

[39] A. Wei, D. Chen, N. Ke, S. Peng and S. P. Wong, 'Characteristics of carbon nitride films prepared by magnetic filtered plasma stream', Thin Solid Films 323, pp. 217-221 (1998).

[40] E. I. Liu, X. Shi, H. S. Tan, L. K. Cheah, Z. Sun, B. K. Tay and J. R. Shi, 'The effect of nitrogen on the mechanical properties of tetrahedral

amorphous carbon films deposited with a filtered cathodic vacuum arc' ,Surf. Coat. Technol. 120, pp. 601-606 (1999).

[41] P. J. Martin, A. Bendavid, R. P. Netterfield, T. J. Kinder, F. Jahan and G. Smith, 'Plasma deposition of tribological and optical thin film materials with a filtered cathodic arc source', Surf. Coat. Technol. 112, pp. 257-260 (1999).

[42] M. Keidar, I.I. Beilis, I.G. Brown, 'Multiply charged ion transport in free boundary vacuum arc plasma jet', J. Appl. Phys. 84, 5956 (1998).

[43] B.K. Tay, Z.W. Zhao, D.H.C. Chua, 'Review of metal oxide films deposited by filtered cathodic vacuum arc technique', Mat. Sci. & Eng. R52, pp. 1-48 (2006).

[44] W.D. Davis, H.C. Miller, 'Analysis of the Electrode Products Emitted by dc Arcs in a Vacuum Ambient', J. Appl. Phys 40, 2212 (1969).

[45] G.Y. Yushkov, E.M. Oks, A. Anders, I.G. Brown, 'Effect of multiple current spikes on the enhancement of ion charge states of vacuum arc plasmas', J. Appl. Phys. 87, 8345 (2000).

[46] W. D. Yu, X. M. Li, X. D. Gao, 'Self-catalytic synthesis and photoluminescence of ZnO nanostructures on ZnO nanocrystal substrates', Appl. Phys. Lett. 84, 2658 (2004).

[47] M. H. Huang, S. Mao, H. Feick, H. Yan, Y. Wu, H. Kind, E. Weber, R. Russo, P. Yang, 'Room-Temperature Ultraviolet Nanowire Nanolasers', Science 292, 1897 (2001).

[48] L. E. Greene, M. Law, D. H. Tan, M. Montano, J. Goldberger, G. Somorjai, P. Yang, 'General Route to Vertical ZnO Nanowire Arrays Using Textured ZnO Seeds', Nano Lett. 5, 1231 (2005).

[49] Y. Hou, M. Yang, G. S. Pang, and S. H. Feng, 'The influence of annealing atmosphere on the optical properties of Flower-like ZnO', Angew. Chem. 115, 3030 (2003).

[50] C. Ye, X. Fang, Y. Hao, X. Teng, L. Zhang, 'Zinc Oxide Nanostructures: Morphology Derivation and Evolution', J. Phys. Chem. B 109, 19758 (2005).

[51] Z.Q. Li, Y. Xie, Y.J. Xiong, R. Zhang, and W. He, 'Reverse micelle-assisted route to control diameters of ZnO nanorods by selecting different precursors' Chem. Lett. **32**(8): pp. 760-761 (2003).

[52] Z.R. Tian, J. Liu, and J.A. Voigt, 'Solution-based synthesis of ordered nanostructures', American Chemical Society **228**, pp. U782-U782 (2004).

[53] L. Vayssieres, 'Growth of arrayed nanorods and nanowires of ZnO from aqueous solutions' Adv. Mat. **15**(5): p. 464-466 (2003).

[54] M. Yin, Y. Gu, I.L. Kuskovsky, T. Andelman, Y. Zhu, G.F. Neumark, and S. O'Brien, 'Zinc oxide quantum rods', J. of the American Chem. Soc. **126**(20): p. 6206-6207 (2004).

[55] G. C. Yi, C. R. Wang and W. I. Park, 'ZnO nanorods: synthesis, characterization and applications', Semicond. Sci. Technol. 20, S22–S34 (2005).

[56] T. Minami, M. Tanigava, M. Yamanishi, T. Kawamura, 'Observation of Ultraviolet-Luminescence from the ZnO MIS Diodes', Jpn. J. Appl. Phys. 13, 1475 (1974).J

[57] T. Aoki, Y. Hatanaka, D. C. Look, 'ZnO diodes fabricated by excimer-laser doping', Appl. Phys Lett. 76, 3257 (2000).J

[58] W. Z. Xu, Z. Z. Ye, Y. J. Zeng, L. P. Zhu, B. H. Zhao, L. Jiang, J. G. Lu, H. P. He, S. B. Zhang, 'ZnO light-emitting diode grown by plasma-assisted metal organic chemical vapor deposition', Appl. Phys. Lett. 88, 173506 (2006).

[59] L. J. Mandalapu, Z. Yang, S. Chu, and J. L. Liua, 'Ultraviolet emission from Sb-doped p-type ZnO based heterojunction light-emitting diodes', Appl. Phys. Lett. 92,122101 (2008).

[60] D. K. Hwang, S. H. Kang, J. H. Lim, E. J. Yang, J. Y. Oh, J. H. Yang, and S. J. Park, 'p-ZnO/n-GaN heterostructure ZnO light-emitting diodes,' Appl. Phys. Lett. 86, 222101 (2005).

[61] A. Tsukazaki, A. Ohtomo, T. Onuma, M. Ohtani, T. Makino, M. Sumiya, K. Ohtani, S. F. Chichibu, S. Fuke, Y. Segawa, H. Ohno, H. Koinuma, M. Kawasaki, 'Repeated temperature modulation epitaxy for p-type doping and light-emitting diode based on ZnO' Nat. Mater. 4, 42 (2005).

[62] T. Ohashi, K. Yamamoto, A. Nakamura, and J. Temmyo, 'Red emission from ZnO-based double heterojunction diode', Jpn. J. Appl. Phys. 47, no. 4, pp. 2961–2964 (2008).

[63] A. Osinsky, J. W. Dong, M. Z. Kauser, B. Hertog, A. M. Dabiran, P. P. Chow, S. J. Pearton, O. Lopatiuk, and L. Chernyak, 'MgZnO/AlGaN heterostructure light-emitting diodes', Appl. Phys. Lett. 85, no. 19, pp. 4272–4274 (2004).

[64] T. A. Edison, US Patent, 484582 (1892).

[65] M. Kikushi, S. Nagakura, H. Ohmura, S. Oketani, Jpn. J. Appl. Phys. 4

(1965) 940.

[66] H. Brandolf, US Patent 4511593 (1985).

[67] I.I. Aksenov, V.G. Padalka, N.S. Repalov, V.M. Khoroshikh, Sov. J. Plasma Phys. 6 (1980) 173.

[68] V. I. Gorokhovsky, US Patent 5435900 (1995).

[69] R. P. Welty, US Patent 5480527 (1996).

[70] T. A. Polley and W. B. Carter, “Zone model for zinc oxide deposited by combustion chemical vapor deposition”, This Solid Films 384, 177 (2001).

[71] M. Chen, Z. L. Pei, X. Wang, C. Sun, and L. S. Wen, “Structural, electrical, and optical properties of transparent conductive oxide ZnO:Al films prepared by dc magnetron reactive sputtering”, J. Vac. Sci. Technol. A **19**, 963 (2001).

[72] V. Gupta and A. Mansingh, “Influence of postdeposition annealing on the structural and optical properties of sputtered zinc oxide film”, J. Appl. Phys. 80, 1063 (1996).

[73] K. C. Park, D. Y. Ma and K. H. Kim, “The physical properties of Al-doped zinc oxide films prepared by RF magnetron sputtering”, Thin Solid Films **305**, 201 (1997).

[74] Z. Q. Xu, H. Deng, Y. Li and H. Cheng, “Al-doping effects on structure, electrical and optical properties of *c*-axis-orientated ZnO:Al thin films”, Material Science in Semiconductor Processing 9, 132-135 (2006).

[75] N. Ohashi, T. Ishigaki, N. Okada, T. Sekiguchi, I. Sakaguchi, and H. Haneda, “Effect of hydrogen doping on ultraviolet emission spectra of

various types of ZnO", Appl. Phys. Lett. 80, 2869 (2002).

[76] E. S. Shim, H. S. Kang, S. S. Pang, J. S. Kang, I. Yun and S. Y. Lee, "Annealing effect on the structural and optical properties of ZnO thin film on InP", Materials Science and Engineering B 102, 366-369 (2003).

[77] G. Lash and F.Stern, "Spontaneous and Stimulated Recombination Radiation in Semiconductors", Phys. Rev. 133, A553 (1964).

[78] A. Tsukazaki et al, M. Kubota, A. Ohtomo, T. Onuma, K. Ohtani, H.Ohno, Shigefusa F. Chichibu and M. Kawasaki, 'Blue light-emitting diode based on ZnO', Jap. J. of Appl. Phys, Vol. 44, No. 21, pp. L 643–L 645 (2005).

[79] J. B. You, X. W. Zhang, S. G. Zhang, H. R. Tan, J. Ying, Z. G. Yin, Q. S. Zhu and Paul K. Chu, 'Electroluminescence behavior of ZnO/Si heterojunctions: Energy band alignment and interfacial microstructure', J. of Appl. Phys 107, 083701 (2010).

[80] P. L. Chen, X. Y. Ma, and D. R. Yang, 'Ultraviolet electroluminescence from ZnO/*p*-Si heterojunctions', J. Appl. Phys. 101, 053103 (2007).

[81] J. Y. Lee, J. H. Lee, H. S. Kim, C. H. Lee, H. S. Ahn, H. K. Cho, Y. Y. Kim, B. H. Kong and H. S. Lee, 'A study on the origin of emission of the annealed *n*-ZnO/*p*-GaN heterostructure LED', Thin Solid Films 517 pp. 5157–5160 (2009).

[82] H. Zhu, C. X. Shan, B. Yao, B. H. Li, J. Y. Zhang, Z. Z. Zhang, D. X. Zhao, D. Z. Shen, X. W. Fan, Y. M. Lu and Z. K. Tang, 'Ultralow-threshold laser realized in zinc oxide', Adv. Mat. 21, 1613, (2009).

[83] C. Yuen, S. F. Yu, S. P. Lau, Rusli, and T. P. Chen, 'Fabrication of *n*-

ZnO:Al/*p*-SiC(4H) heterojunction light-emitting diodes by filtered cathodic vacuum arc technique', Appl. Phys. Lett. 86, 241111, (2005).

[84] S. M. Sze, Physics of Semiconductor Devices, Wily, New York (1981).

[85] Ya. I. Alivov, J. E. Van Nostrand, D. C. Look, M. V. Chukichev B. M. Ataev, 'Observation of 430 nm electroluminescence from ZnO/GaN heterojunction light-emitting diodes', Appl. Phys Lett, 83, 14 (2003).

[86] D. J. Rogersa, F. H. Teherani, A. Yasan, K. Minder, P. Kung and M. Razeghi, "Electroluminescence at 375 nm from a ZnO/GaN:Mg/*c*-Al_2O_3 heterojunction light emitting diode", Appl. Phys. Lett. 88, 141918, 2006.

[87] P. L. Chen, X. Y. Ma and D. R. Yang, "Fairly pure ultraviolet electroluminescence from ZnO-based light-emitting devices", Appl. Phys. Lett 89, 111112 (2006).

[88] Z. P. Wei, Y. M. Lu, D. Z. Shen, Z. Z. Zhang, B. Yao, B. H. Li, J. Y. Zhang, D. X. Zhao, X. W. Fan, and Z. K. Tang, 'Room temperature *p-n* ZnO blue-violet light-emitting diodes', Appl. Phys. Lett. 90, 042113 (2007).

[89] L. Eckey, U. von Gfug, J. Holst, A. Hoffmann, A. Kaschner, H. Siegle, C. Thomsen, B. Schineller, K. Heime, M. Heuken, O. Schön, and R. Beccard, 'Photoluminescence and Raman study of compensation effects in Mg-doped GaN epilayers', J. Appl. Phys 84, 5828 (1998).

[90] Y. Li, G. W. Meng, L. D. Zhang, and F. Phillipp, 'Ordered semiconductor ZnO nanowire arrays and their photoluminescence properties', Appl. Phys. Lett. 76 (15) pp 2011-2013 (2000).

[91] W.I. Park, D.H. Kim, S.W. Jung, and G.C. Yi, 'Metalorganic vapor-

phase epitaxial growth of vertically well-aligned ZnO nanorods', Appl. Phys. Lett. 80 (22), pp 4232-4234 (2002).

[92] J.H. Guo, L. Vayssieres, C. Persson, R. Ahuja, B. Johansson, and J. Nordgren, 'Polarization-dependent soft-x-ray absorption of highly oriented ZnO microrod Arrays', Journal of Physics-Condensed Matter, 14(28) pp 6969-6974 (2002).

[93] Y.B. Li, Y. Bando, T. Sato, and K. Kurashima, 'ZnO nanobelts grown on Si Substrate', Appl. Phys. Lett., 81(1), pp 144-146 (2002).

[94] Z.W. Pan, Z.R. Dai, and Z.L. Wang, 'Nanobelts of semiconducting oxides', Science, 291(5510), pp 1947-1949 (2001).

[95] J.Q. Hu, Q. Li, X.M. Meng, C.S. Lee, and S.T. Lee, 'Thermal reduction route to the fabrication of coaxial Zn/ZrO nanocables and ZnO nanotubes', Chemistry of Materials, 15(1) pp 305-308 (2003).

[96] S. H. Park, S. H. Kim, and S. W. Han, 'Growth of homoepitaxial ZnO film on ZnO nanorods and light emitting diode applications', Nanotechnology Vol. 18, no. 5, pp 055 608 (2007).

[97] C. Y. Chang, F. C. Tsao, C. J. Pan, G. C. Chi, H. T. Wang, J. J. Chen, F. Ren, D. P. Norton, S. J. Perton, K. H. Chen, and L. C. Chen, 'Electroluminescence from ZnO nanowire/polymer composite p-n junction',Appl. Phys. Lett. 88, No. 17 173503 (2006).

[98] R. Guo, J. Nishimura, M. Matsumoto, M. Higshihata, D. Nakamura, and T. Okada, 'Electroluminescence from ZnO nanowires based p-GaN/n-ZnO heterojunction light-emitting diodes', Appl. Phys. B, Photophys. Laser Chem. 94, no. 1, pp 33–38, (2009).

[99] Y. Y. Xi, Y. F. Hsu, A. B. Djurisic, A. M. C. Ng, W. K. Chan, H. L.

Tam, and K. W. Cheah, ‘NiO/ZnO light emitting diodes by solution-based growth’, Appl. Phys. Lett. 92, No. 11, 113505 (2008).

[100] H.J. Fan, W. Lee, R. Scholz, A. Dadgar, A. Krost, K. Nielsch, and M. Zacharias, ‘Arrays of vertically aligned and hexagonally arranged ZnO nanowires: a new template-directed approach’, Nanotechnology 16 (6) pp 913-917 (2005).

[101] L. L. Yang, Q. X. Zhao, M. Willander, J. H. Yang, and I. Ivanov, ‘Annealing effects on optical properties of low temperature grown ZnO nanorod arrays’ J. Appl. Phys. 105, 053503 (2009).

[102] J. H. Lang, Q. Han, C. S. Li, J. H. Yang, X. Li, L. L. Yang, D. D. Wang, H. J. Zhai, M. Gao, Y. J. Zhang, X. Y. Liu, and M. B. Wei, ‘Effect of Mn doping on the microstructures and photoluminescence properties of CBD derived ZnO nanorods’, Appl. Surf. Sci. 256, 3365 (2010).

[103] B. K. Choi, D. H. Chang, Y. S. Yoon, and S. J. Kang, ‘Optical characterization of ZnO thin films deposited by Sol-gel method’, J. Mater. Sci. Vol. 17, 12, pp 1011-1015 (2006).

[104] K. Vanheusden, W. L. Warren, C. H. Seager, D. K. Tallant, J. A. Voigt, and B. E. Gnade, ‘Mechanisms behind green photoluminescence in ZnO phosphor powders’, J. Appl. Phys. 79, 7983 (1996).

[105] T. F. Chung, J. A. Zapien, and S. T. Lee, “Luminescent Properties of ZnO Nanorod Arrays Grown on Al:ZnO Buffer Layer”, J. Phys. Chem. C 112 (3), pp 820-824 (2008).

[106] A. R. Kim, J. Y. Lee, B. R. Jang, H. S. Kim, Y. J. Cho, H. K. Park, N. W. Jang, and J. H. Kim, ‘Effect of Buffer Layer Thickness on the

Growth Properties of Hydrothermally Grown ZnO Nanorods', J. Nanosci. Nanotechnol. Vol. 11, No. 2 (2011).

[107] Ya. I. Alivov, J. E. Van Nostrand, D. C. Look, 'Observation of 430 nm electroluminescence from ZnO/GaN heterojunction light-emitting diodes' M. V. Chukichev and B. M. Ataev, Appl. Phys. Lett. 83, No. 14 pp. 2943-2945 (2003).

[108] H. Long, G. J. Fang, H. H. Huang, X. M. Mo, W. Xia, B. Z. Dong, X. Q. Meng and X. Z. Zhao, 'Ultraviolet electroluminescence from ZnO/NiO-based heterojunction light-emitting diodes', Appl. Phys. Lett. 95, 013509 (2009)

[109] Y.T. Shih, M.K. Wu, M.J. Chen, Y.C. Cheng, J.R. Yang and M. Shiojiri, 'ZnO-based heterojunction light-emitting diodes on *p*-SiC(4H) grown by atomic layer deposition', Appl. Phys. B, DOI 10.1007/s00340-009-3809-0 (2009).

[110] D. C. Kim, W. S. Han, H. K. Cho, B. H. Kong, and H. S. Kim, 'Multidimensional ZnO light-emitting diode structures grown by metal organic chemical vapor deposition on *p*-Si', Appl. Phys. Lett. 91, 231901 (2007).

[111] Eunice S. P. Leong and S. F. Yu, 'UV Random Lasing Action in p-SiC(4H)/i-ZnO–SiO2 Nanocomposite/n-ZnO:Al Heterojunction Diodes', Adv. Mat. 18, 1685-1688 (2006).

[112] S. Zhao, Z. Xu, F. Zhang, W. Jiang, J. Huang, Y. Wang and X. Xu, 'Schematic design of a complex thin-film luminescent screen usable for vacuum fluorescent and field emission display', Optics Letter 32 (5), 2094–2096 (2007).

[113] H. J. Bolink, E. Coronado, D. Repetto, and M. Sessolo, ‘Air stable hybrid organic-inorganic light emitting diodes using ZnO as the cathode’, Appl. Phys. Lett. 91, 223501 (2007).

[114] S. L. Zhao, P. Z. Kan, Z. Xu, C. Kong, D. W. Wang, Y. Yan and Y. S. Wang, ‘Electroluminescence of ZnO nanorods/MEH-PPV heterostructure devices’, Organic Electronics 11, 789–793 (2010).

[115] N. Bano, S. Zaman, A. Zainelabdin, S. Hussain, I. Hussain, O. Nur, and M. Willander, ‘ZnO-organic hybrid white light emitting diodes grown on flexible plastic using low temperature aqueous chemical method’, J. Appl. Phys. 108, 043103 (2010).

[116] C. Y. Chang, F. C. Tsao, C. J. Pan, G. C. Chi, H. T. Wang, J. J. Chen, F. Ren, D. P. Norton, S. J. Pearton, K. H. Chen, and L. C. Chen, ‘Electroluminescence from ZnO nanowire/polymer composite *p-n* junction’, Appl. Phys. Lett. 88, 173503 (2006).

[117] R. Könenkamp, R. C. Word, and C. Schlegel, ‘Vertical nanowire light-emitting diode’, Appl. Phys. Lett. 85, 6004 (2004).

[118] M Willander, O Nur, Q X Zhao, L L Yang, M Lorenz, B Q Cao, J Zúñiga Pérez, C Czekalla, G Zimmermann, M Grundmann, A Bakin, A Behrends, M Al-Suleiman, A El-Shaer, A Che Mofor, B Postels, A Waag, N Boukos, A Travlos, H S Kwack, J Guinard and D Le Si Dang, ‘Zinc oxide nanorod based photonic devices: recent progress in growth, light emitting diodes and lasers’, Nanotechnology 20, 332001 (2009).

[119] L. E. Greene, M. Law, J. Goldberger, F. Kim, Justin C. Johnson, Yanfeng Zhang, Richard J. Saykally, and Peidong Yang, ‘Low temperature wafer-scale production of ZnO nanowires arrays’, Angew.

Chem. Int. Edition 42, 3031-3034 (2003).

[120] L. Vayssieres, ‘Growth of Arrayed Nanorods and Nanowires of ZnO from Aqueous Solutions’, Adv. Mat. 15, No. 5 (2003).

[121] A. Nadarajah, R. C. Word, J. Meiss, and R. Könenkamp, ‘Flexible Inorganic Nanowire Light-Emitting Diode’ Nanoletters, Vol. 8, No. 2, 534-537 (2008).

[122] H. Lee, S. W. Cho, K. Han, P. E. Jeon, C. N. Whang, K. Jeong, K. Cho and Y. Yi, ‘The origin of the hole injection improvements at indium tin oxide/molybdenum trioxide/*N*,*N*′-bis(1-naphthyl)-*N*,*N*′-diphenyl-1,1′-biphenyl- 4,4′-diamine interfaces’, Appl. Phys. Lett. 93, 043308 (2008)

[123] C. H. Huang, F. Y. Li and W. Huang, Introduction to Organic Light-emitting Materials and Devices, pp. 64-65 (2005).

[124] A. B. Djurišić, Y. H. Leung, K.H. Tam, Y. F. Hsu, L. Ding, W. K. Ge, Y. C. Zhong, K. S. Wong, W. K. Chan, H. L. Tam, K. W. Cheah, W. M. Kwok and D. L. Phillips, ‘Defect emissions in ZnO nanostructures’, Nanotechnology 18**,** 095702 (2007).

[125] K.A. Osipov, V.N. Pavlovskii, E.V. Lutsenko, A.L. Gurskii, G.P. Yablonskii, S. Hartmann, A. Janssen, H. H. Johannes, R. Caspary, W. Kowalsky, N. Meyer, M. Gersdorff, M. Heuken, P. van Gemmern, C. Zimmermann, F. Jessen, H. Kalisch and R.H. Jansen, ‘Influence of thermal annealing on photoluminescence and structural properties of *N*,*N*′-diphenyl-*N*,*N*′-bis(1-naphthylphenyl)-1,1′-biphenyl-4,4′-diamine (α-NPD) organic thin films’, Thin Solid Films 515, 4834-4837 (2007).

[126] Y. M. Sun, Ph.D. thesis, University of Science and Technology of

China, (2000).

[127] J. D. Ye, S. L. Gu, S. M. Zhu, W. Liu, S. M. Liu, R. Zhang, Y. Shi, and Y. D. Zheng, 'Electroluminescent and transport mechanisms of *n*-ZnO/*p*-Si heterojunctions', Appl. Phys. Lett. 88, 182112 (2006).

[128] P. L. Chen, X. Y. Ma and D. Yang, 'Ultraviolet electroluminescence from ZnO/*p*-Si heterojunctions', J. Appl. Phys. 101, 053103 (2007).

[129] S. W. Lee, H. D. Cho, G. Panin and T. W. Kang, 'Vertical ZnO nanorod/Si contact light-emitting diode', Appl. Phys. Lett. 98, 093110 (2011).

[130] T. S. Herng, S. P. Lau, S. F. Yu, S. H. Tsang, K. S. Teng and J. S. Chen, 'Ferromagnetic Cu doped ZnO as an electron injector in heterojunction light emitting diodes', J. Appl. Phys. 104, 103104 (2008).

[131] T. Chassw, C. I. Wu, I. G. Hill and A. Kahn, 'Band alignment at organic-inorganic semiconductor interfaces: α-NPD and CuPc on InP(110)', J. Appl. Phys. 85, 6589 (1999).

[132] D. Basko1, G.C. La Rocca1, F. Bassani, and V.M. Agranovich, 'Förster energy transfer from a semiconductor quantum well to an organic material overlayer', The European Physical Journal B 8, 353-362 (1999).

[133] M. Berggren, A. Dodabalapur, R.E. Slusher and Z. Bao, 'Light amplification in organic thin films using cascade energy transfer', Nature 389, 466 (1997).